6.Numerical Modelling

6.1. Introduction

The Abaqus software was selected to numerically model the wafer using the finite element method. Two different techniques were used to simulate the deformation behaviour of the wafer. In the first method, the wafer was represented with a simple repetitive geometry but given a complex foam material model within the software's material database. The second method used the actual architecture obtained from the X-ray tomographic scan to generate a 3D geometry of the wafer. A simple linear elastic material model was then used for the solid parts of the wafer. It was desired to simulate the deformation beyond the elastic region so a damage criterion was implemented to represent the fracture of the cell walls. Verification of the finite element analysis was performed by comparison to the load output and visual data obtained from in-situ experiments.

6.2. Idealised Wafer Geometry

6.2.1. Uni-axial Compression Model

A solid three dimensional model of the wafer sheet was generated on Solidworks [113] using the dimensions measured from optical microscopy in Section 4.3.1. Since the experimental compression specimen was circular, symmetry was utilised and thus only a quarter of the geometry was modelled. This idealized geometry was then imported into Abaqus for analysis. It was partitioned into the skin and core sections and each was assigned the different linear elastic material properties obtained from the analytical calculations of Chapter 5.3.3. The dimensions of the skin and core partitions were based on the optical micrographs, rather than from the scanning electron micrographs for simplicity, and the model can be seen in Figure 6.1.

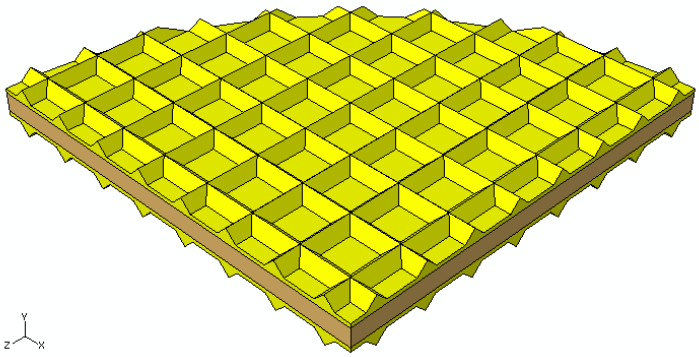

Figure 6.1 Idealised geometry model with the skin (yellow) and core (brown) sections

The meshed model consisted of 155088 tetrahedral linear elements. Symmetrical boundary conditions were applied to the flat faces which were parallel to the loading direction. The compression was simulated in two ways, by displacing the top edges of the reedings (Figure 6.2a) and by displacing a rigid body to contact the wafer (Figure 6.2b). The skin and core were given randomly chosen linear elastic material properties with Young's modulus values of 1000 MPa and 2 MPa respectively, since this simulation was only to determine the best method of loading the model.

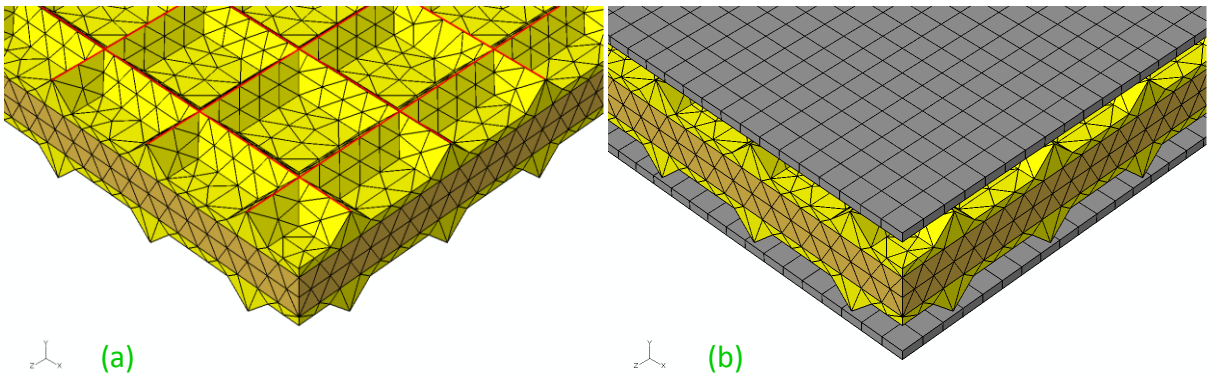

Figure 6.2 The model compressed by a) displacing the edges of the reedings and b) rigid body plates

In the compression simulation represented in Figure 6.2a, the load was calculated by summing the reaction forces at the nodes along the top edge of the reedings. In the compression simulation represented in Figure 6.2b, the load was given by a single reaction force acting through a reference point of the rigid plate. The results in Figure 6.3 showed that the load-displacement output was the same for both methods of compression. The initial

horizontal part of the graph obtained from the model compressed with the two plates was due to the initial displacement of the plates before coming into contact with the wafer model. For simplicity, the displacement of the reedings method was used for future compression models.

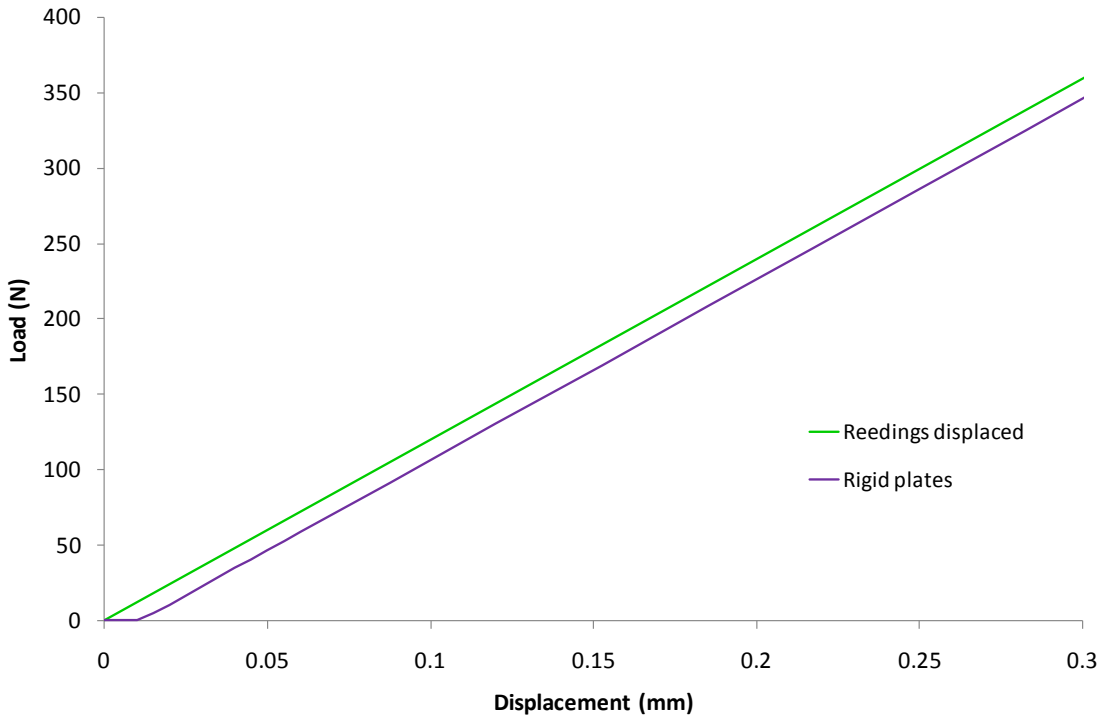

Figure 6.3 The load-displacement graphs of a wafer compressed by displacing the top edge of reedings and by rigid body plates

The skin and core regions were subsequently assigned the Young's modulus values of 1150 MPa and 0.722 MPa which were calculated analytically in Section 5.3.3. The top edges of the reedings of the wafer model were then displaced to simulate compression. The FE output was compared to the experimental stress-strain curves of a single circular wafer sheet obtained in Section 3.2.6. Figure 6.4 shows the deformation plots of the experimental compression and the finite element simulation. Since the skin and core regions of the model were not given any damage criterion, only the elastic region of the compression was analysed. The wafer compression modulus predicted by the model was 1.83 MPa which was higher than the experimentally measured value of 1.32 MPa. An inverse analysis was

performed by varying the input modulus of the core region. A value of 0.52 MPa for the core modulus resulted in an apparent compression modulus which was closer to the experimental value as shown by the blue curve in Figure 6.4. The analytical and numerical predictions for the core modulus differed because the analytical equation for compression (Equation 5.12) does not account for the geometry of the reedings. It could be shown that if the modulus of the skin in the model was varied, there was negligible effect on the apparent compressive modulus. When the experimentally obtained modulus of 1.32 MPa from Chapter 3.2.6 was input into the entire wafer model, the apparent compression modulus was underpredicted (yellow curve). This was to be expected since the experimental apparent compressive modulus was calculated using the maximum height between reedings and did not consider the variable geometry due to the grid of reedings.

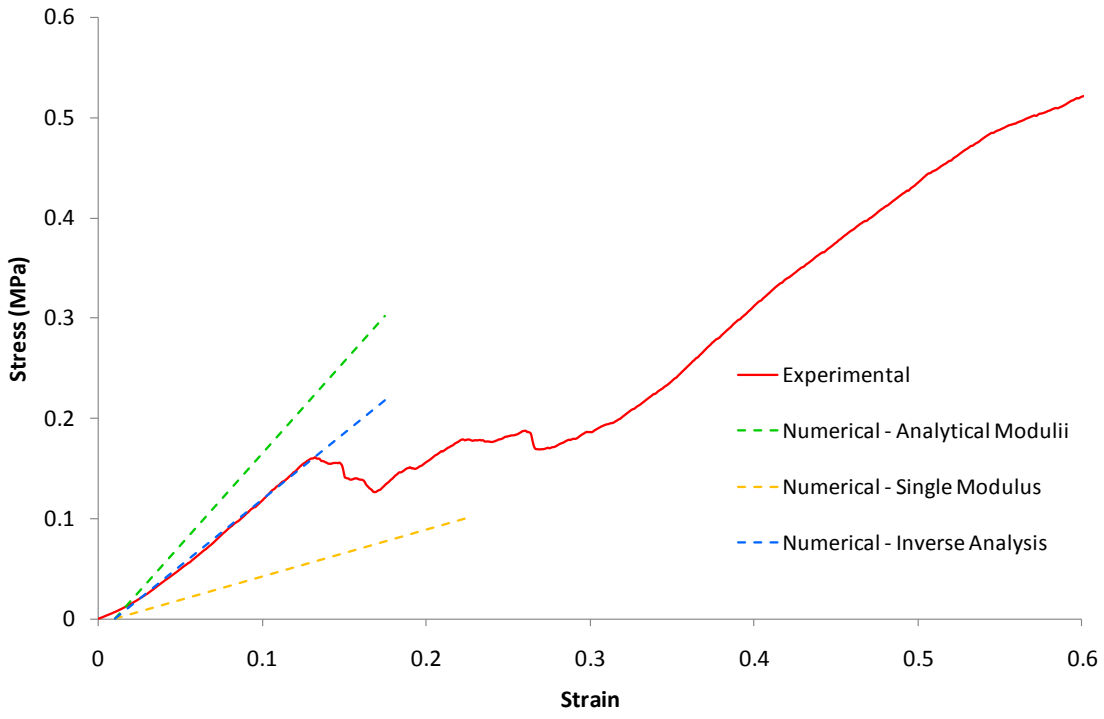

Figure 6.4 The stress-strain output of the numerical model using the analytically calculated modulii compared to the experimental compression graph

6.2.2. Three Point Bending Model

The wafer was next modelled in flexure. As with the compression model, the wafer was partitioned into the skin are core regions, each with their respective Young's modulii of 1150 MPa and 0.722 MPa respectively. The dimensions of the model (120 x 15 mm) were selected based on the bending experiments performed in Section 3.3. The geometry of the model was simplified to half the length due to symmetry and one-sixth of the width due to the repetitive pattern of the reedings. Symmetrical boundary conditions were given to the central face as highlighted green in Figure 6.5. The wafer beam was also displaced at the point indicated by the red arrow and fixed at the reeding edge indicated by the green arrow in Figure 6.5.

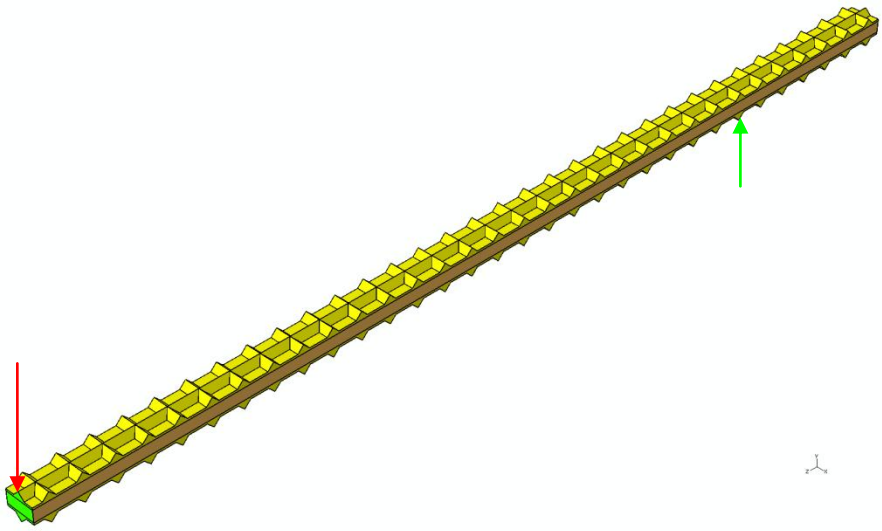

Figure 6.5 The wafer beam model used to simulate bending

The load-displacement output from the Abaqus simulation was plotted in Figure 6.6 and compared to the load-displacement data obtained from the three point bending experiments of Section 3.3. The stiffness gradient output from the model was 0.062 N/mm which was less than the experimentally measured value of 0.075 N/mm. An inverse analysis was performed by modifying the skin modulus to a value which would result in the same apparent stiffness which was experimentally observed. This skin modulus value was found to be 1400 MPa which was 20% more than the analytically calculated value 1150 MPa. The discrepancy can again be attributed to simplification of the wafer geometry in the compression Equation

5.12. As discussed in Section 5.3.3, the bending deflection Equation 5.11 was also used to determine a single flexural modulus of the wafer (ie. $E_{skin} = E_{core}$) which was found to be 952 MPa. This value was applied to the finite element model and the load-displacement output was plotted in Figure 6.6 (yellow line). The numerical result compared very well with the experimental deflection, thus verifying the validity of the analytical calculation. However, the major drawback was that the model could not predict the bending deflection at which the wafer beam fractured.

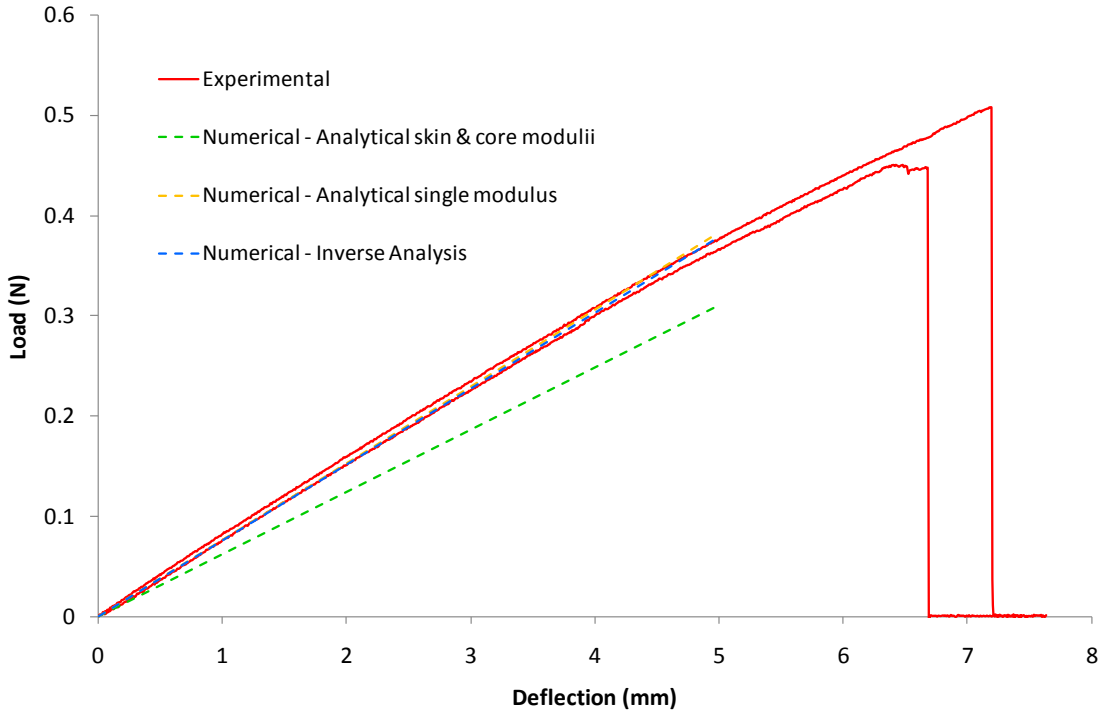

Figure 6.6 The load-displacement output of the numerical model using the analytically calculated modulii compared to the experimental bending graph

6.2.3. Crushable Foam Material Model

Abaqus possesses two foam material models, the “Hyperfoam” from the elastic library and the “Crushable Foam” from the plastic library. The crushable foam plasticity model is intended for the analysis of foams that are used in energy absorption structures and simulates the compressive deformation due to cell wall buckling. The initial elastic part of the deformation is specified by the linear elastic material model while the plastic part of the

behaviour is described by the yield surface which is a von-Mises circle in the deviatoric stress plane and an ellipse in the meridional stress plane [82]. The hardening curve describes the uniaxial compression yield stress as a function of the corresponding plastic strain. There are two hardening models available, volumetric and isotropic.

The shape factor of the yield surface in volumetric and isotropic hardening is calculated using the initial yield stress in uniaxial compression (σ^0_c) and the initial yield stress in hydrostatic compression (p^0_c) while the yield strength in hydrostatic tension (p_t) is also required in the case of volumetric hardening. Calibration of the crushable foam material in Abaqus required the 'compression yield stress ratio' (σ^0_c/p^0_c) as an input variable for both hardening models while the volumetric and isotropic needed additional variables of 'hydrostatic yield stress ratio' (p_t/p^0_c) and plastic Poisson's ratio (v_p) respectively. The hardening law was specified by inputting user-provided data (in tabular form) of the yield stress in uniaxial compression as a function of the axial plastic strain.

6.2.4. Parametric Analysis of the Crushable Foam Material Model

In order to understand the influence of the various input parameters of the crushable foam a single element was analysed and the stress-strain behaviour was recorded. Figure 6.7 shows the loading (red arrows) and symmetrical boundary conditions (green arrows) of the element. A 2-dimensional plane strain element with reduced integration (CPE4R) was used in each case and the NLGEOM function for large displacements was turned on.

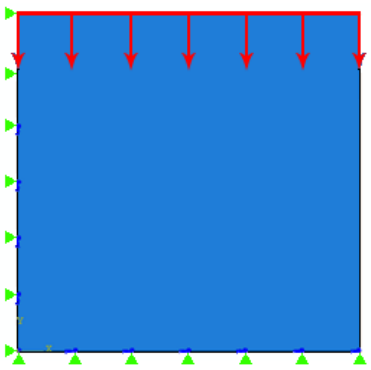

Figure 6.7 Boundary conditions for a single element model

The crushable foam material data was taken from an Abaqus example input file. Each element model was displaced by a fixed amount, hence simulating uniaxial compression or tension. The volumetric hardening model was first investigated by varying the hydrostatic yield stress ratio and keeping the compression yield stress ratio constant at a value of 1.1. As can be seen in Figure 6.8, the stress-strain response did not vary much over three orders of magnitude. In fact, the Abaqus manual recommends using a value of 0.1 since foams are rarely tested in tension [82].

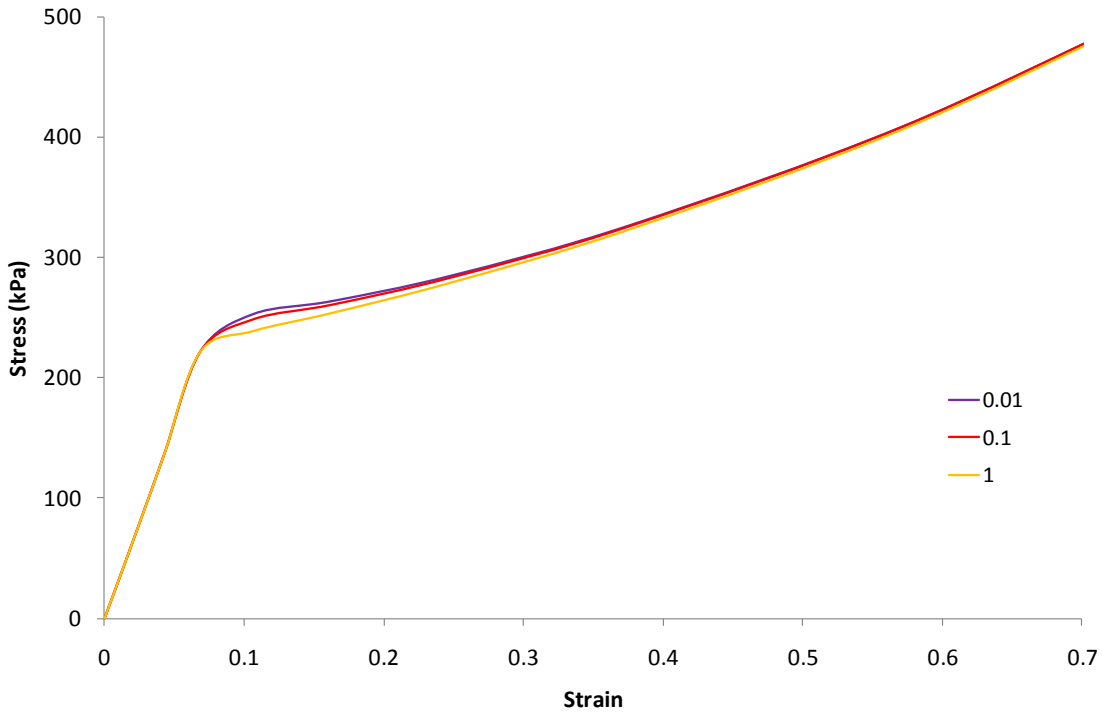

Figure 6.8 Stress-strain response in compression : Hydrostatic yield stress ratio is varied while the Compression yield stress ratio is kept constant at 1.1 (volumetric hardening)

Figure 6.9 shows the stress-strain response as the compression yield stress ratio was varied while the hydrostatic yield stress ratio was kept fixed at 0.1. The initial yield stress decreased as the limit of compression yield stress ratio (3) was approached. However, at lower ratios there seemed to be minimal effect on the deformation even over three orders of magnitude.

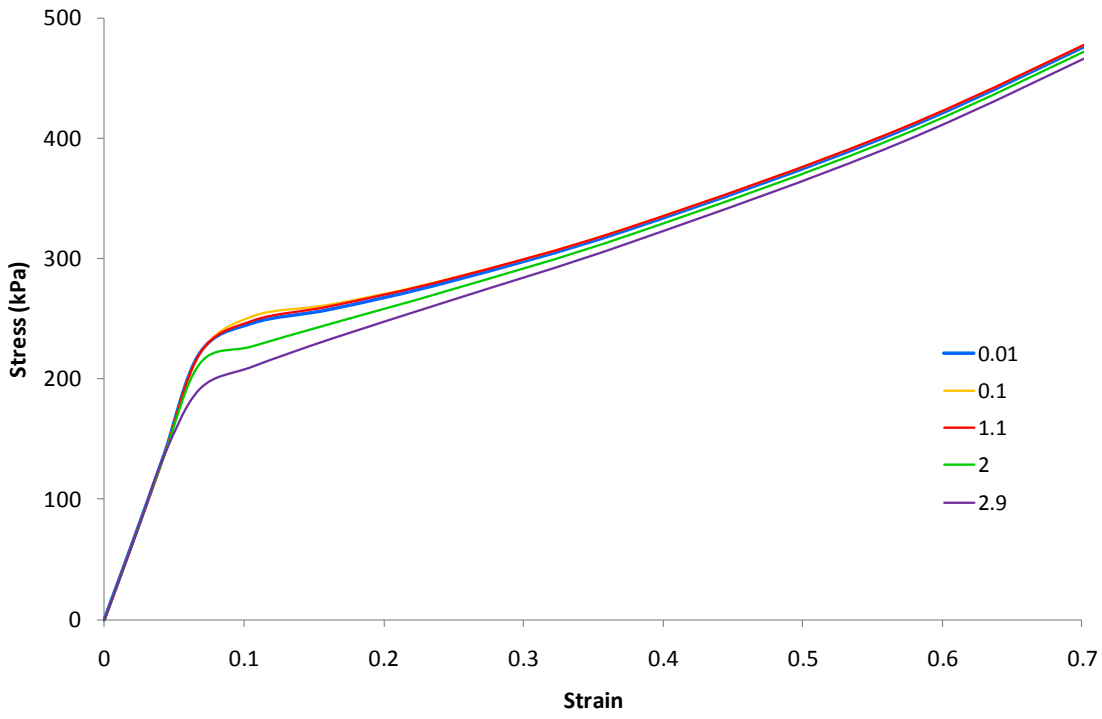

Figure 6.9 Stress-strain response in compression: Compression yield stress ratio is varied while the Hydrostatic yield stress ratio is kept constant at 0.1 (volumetric hardening)

The single element was displaced in tension. The compression yield stress ratio and the hydrostatic yield stress ratio were again varied while one was kept constant to observe the deformation response. The resulting stress-strain curves are shown in Figure 6.10 and Figure 6.11. They indicate that as the compression yield stress ratio is increased, the yield stress in tension decreases whereas if the hydrostatic yield stress ratio is increased, the yield stress in tension is increased. These trends are to be expected since the initial yield stress in uniaxial compression, which was input in the hardening data, is of a fixed magnitude. For a hydrostatic yield stress ratio of 1, the yield stress is the same in compression and tension.

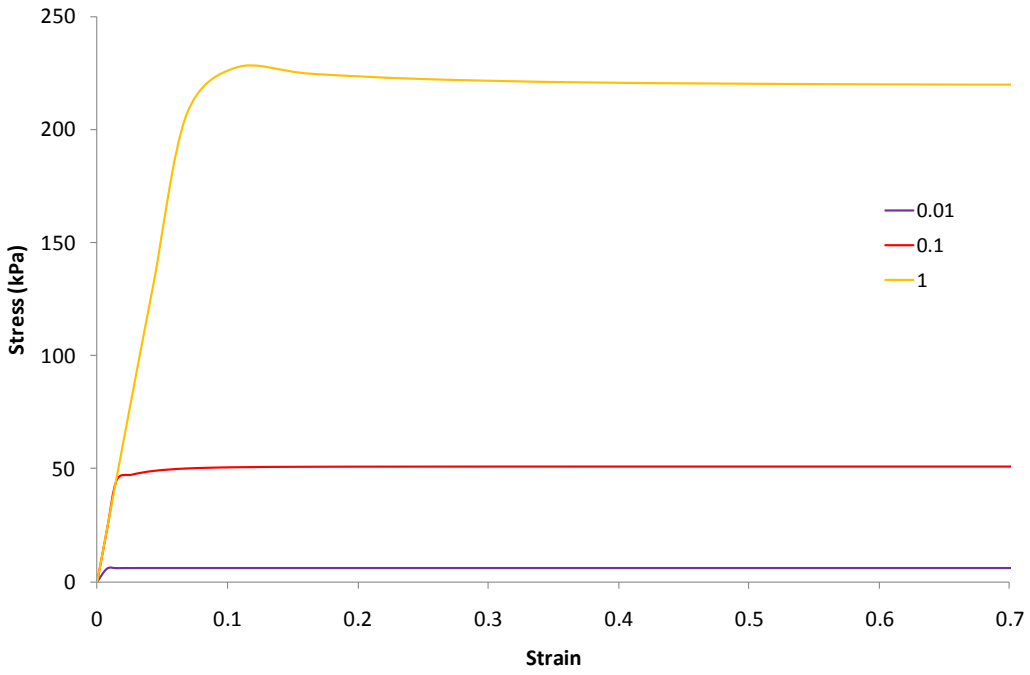

Figure 6.10 Stress-strain response in tension: Hydrostatic yield stress ratio is varied while the Compression yield stress ratio is kept constant at 1.1 (volumetric hardening)

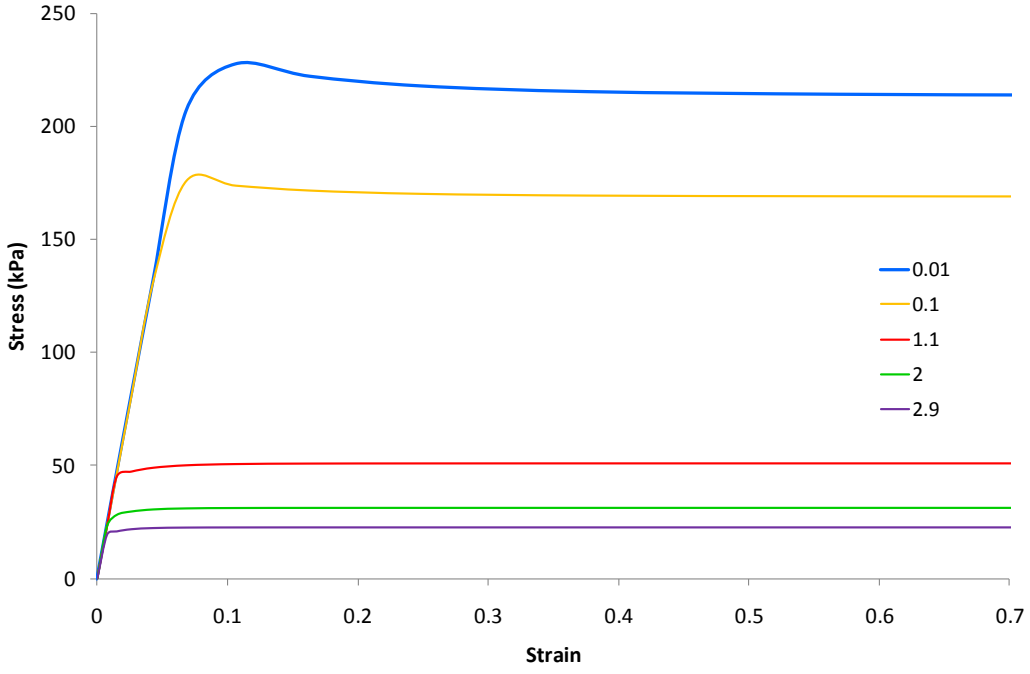

Figure 6.11 Stress-strain response in tension: Compression yield stress ratio is varied while the Hydrostatic yield stress ratio is kept constant at 0.1 (volumetric hardening)

The isotropic hardening model was investigated by varying the plastic Poisson's ratio while keeping the compression yield stress ratio fixed at 1.1. Abaqus allowed a permissible range of values between -1 and 0.5 for the plastic Poisson's ratio, where a value of 0.5 corresponds to incompressible flow. Negative Poisson's ratios are associated with auxetic foams and as can be seen in Figure 6.12, the stress-strain response showed signs of softening after the initial yield. This was reminiscent of the compressive wafer deformation in which there was a drop in stress after the initial fracture.

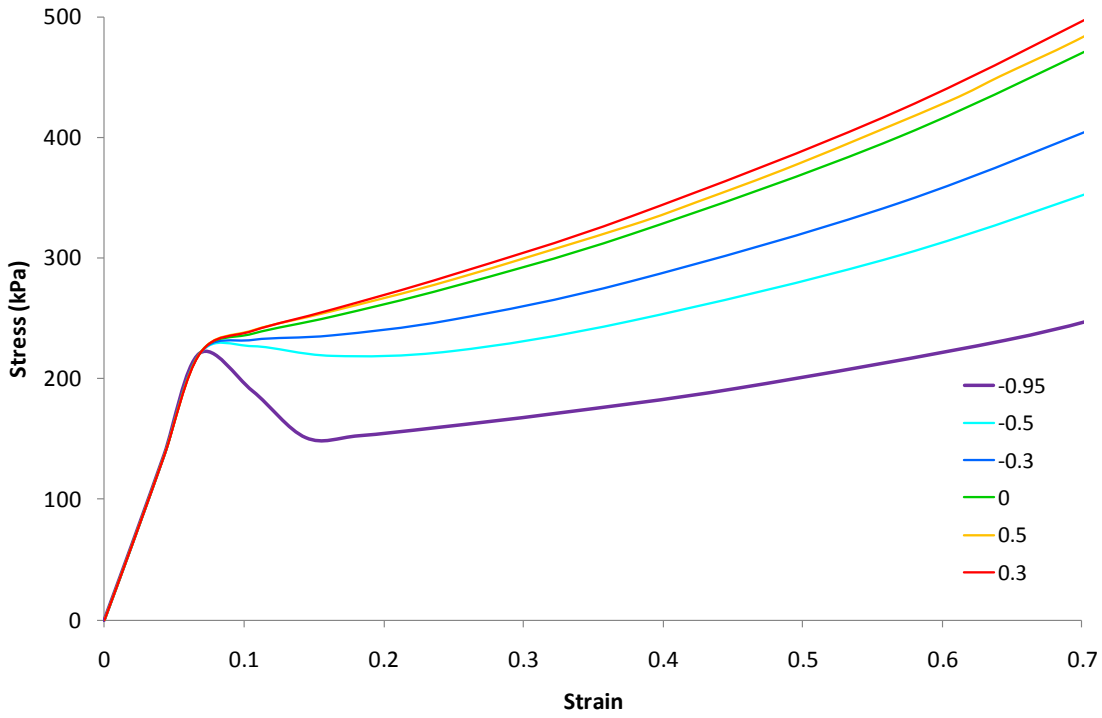

Figure 6.12 Stress-strain response in compression: Plastic Poisson's ratio is varied while the Compression yield stress ratio is kept constant at 1.1(isotropic hardening)

6.2.5. Uni-axial compression of the wafer with the Crushable Foam model

The crushable foam material model was next implemented to the core region so that the deformation beyond the elastic region could be simulated. For this analysis, the modulus values of 0.52 MPa and 1400 MPa for the core and skin respectively, which were determined via the inverse analysis were used. The input parameters were estimated with values of 1.0 and 0.1 for the 'compression yield stress ratio' and 'hydrostatic yield stress ratio' respectively

for the volumetric hardening model. The simulation was also run using the isotropic hardening option with a 'compression yield stress ratio' of 1.0 and plastic Poisson's ratio of 0. The foam hardening was tabulated using selected data points along the stress-strain curve obtained from the experimental uni-axial compression tests. The output load displacement data was used to plot an apparent stress-strain graph in the same manner as for the compression experiments. The FE curve was compared with the experimental curves as shown in Figure 6.13.

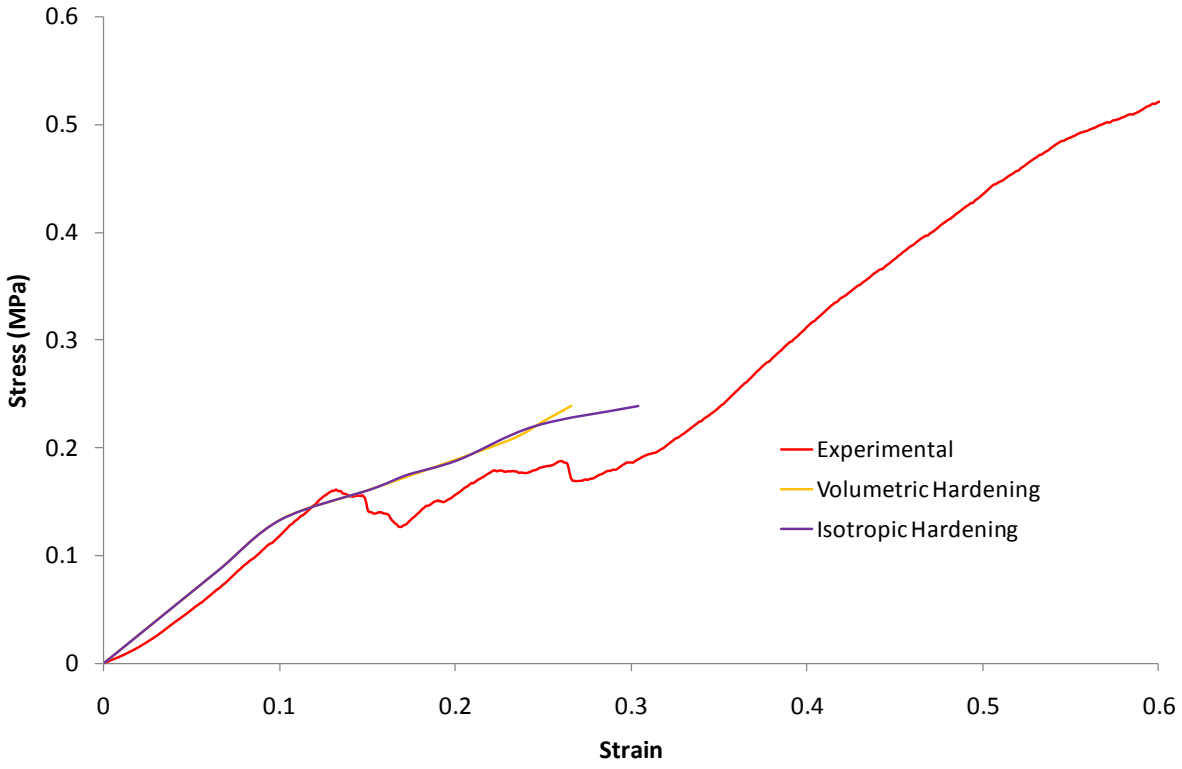

Figure 6.13 The stress-strain response of the finite element compression simulation using the Crushable Foam material model compared to the experimental compression graph

The linear elastic regions were comparable as expected. In the case of the volumetric and isotropic hardening, the plateau region produced a slowly increasing stress as the strain was increased. This region slightly over predicted the experimentally observed stresses. The most noticeable difference was that the experimental curve possessed a jagged pattern due to the progressive fracture of the wafer cell walls while the FE curve was much smoother in nature.

The Crushable Foam material model is intended for rigid foams thus the model works only if the stresses in the tablular hardening data increase as the strain increases. The material model may be able to predict a smoothened trend for a brittle foam but it cannot be used to accurately simulate brittle fracture.

6.3. Actual Wafer Architecture

6.3.1. Mesh Import of Wafer Architecture

An FE model with the geometry of the actual architecture of the wafer was obtained using X-ray microtomography data and 3D visualisation and meshing software. The process from tomographic images to a 3D finite element grid is visualised in Figure 6.14 and a detailed explanation of the mesh generation can be found in Section 4.4. The raw data obtained from the X-ray tomography consisted of 512 image slices, each of 720 x 734 pixels with a resolution of 5µm which represented about 2.5 x 2.5mm of the wafer. Image enhancement was done on ImageJ software before being imported into Avizo software to begin the mesh generation. The image stack was labelled which allowed the construction of a three dimensional volumetric representation of the wafer. A surface consisting of triangles was created to encase the volume and finally a tetrahedral grid was generated to fill the interior of the surface model. The node and element co-ordinates of the 3D grid were exported to an Abaqus input file to begin the quantitative analysis.

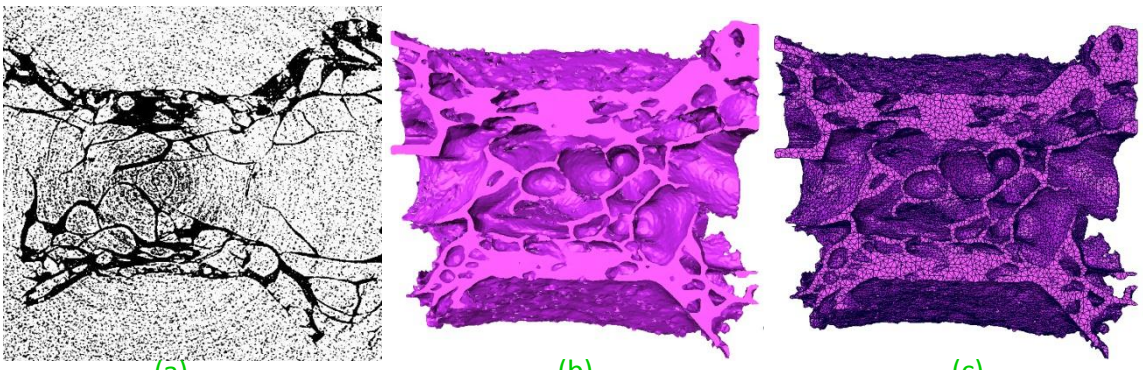

Figure 6.14 XMT scan to mesh grid generation: a) tomographic slices, b) surface volume, c) tetrahedral mesh

6.3.2. Trial Compression Simulation Models

In preliminary studies, only a small portion of the wafer microstructure was modelled for simplicity and to reduce computing time. The region selected can be visualised in Figure 6.15 and represents the "flat" section of the wafer between reedings with dimensions of 1mm x 1mm x 1.3mm. It should be noted that for these preliminary simulations, the dimensions of the models were measured in voxels.

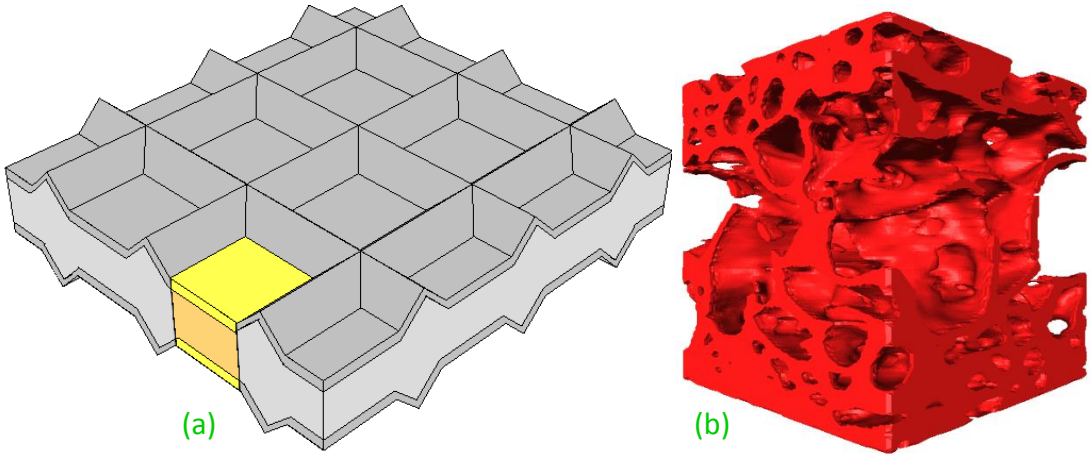

Figure 6.15 The region of the wafer used for the preliminary simulations a) idealized geometry b) actual architecture

It possessed both the designated skin and core regions which made it a suitable model to use in a preliminary compression simulation. The selected volume was re-generated four times, each with a different mesh density so that a convergence test could be performed to determine the influence of the mesh density on the output. The models consisted of 27182, 138205, 394804 and 706543 elements and are shown in Figure 6.16. The Avizo software could not allocate sufficient memory to produce tetrahedral grids with more refined meshes.

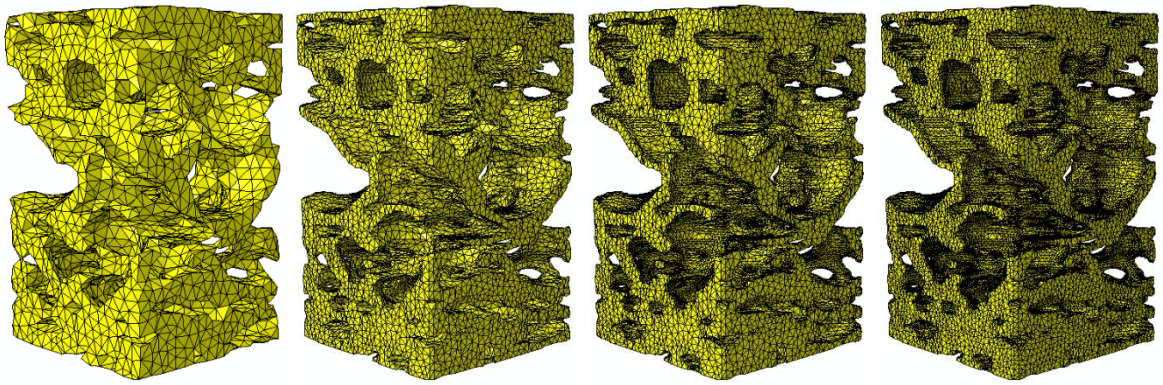

Figure 6.16 A section of the wafer architecture with different levels of mesh refinement

A simple linear elastic material with a Young's modulus of 200 MPa was used to describe solid cell walls of the wafer. This value was chosen based on the analytical calculations in Section 5.4. The surface elements of the upper skin were selected and given a ramped displacement in the z-axis while the bottom surface was kept fixed in the loading direction as seen in Figure 6.17a.

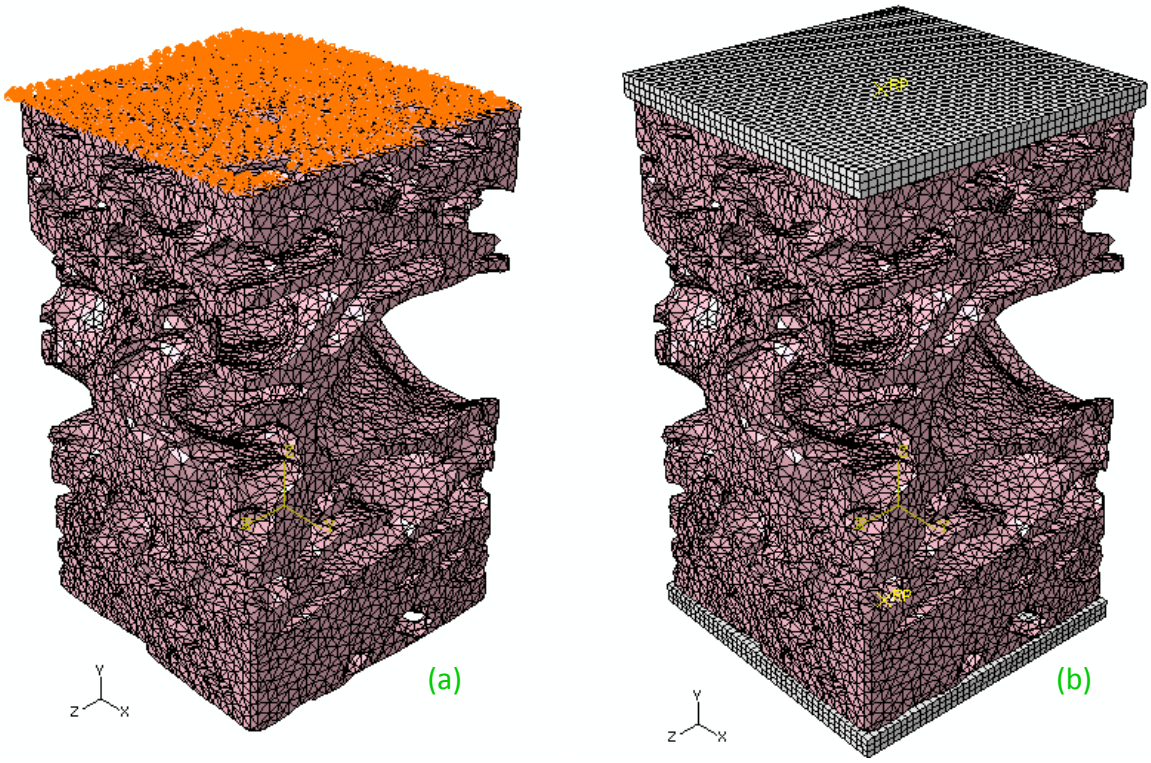

Figure 6.17 The models with different loading conditions a) top surface displaced b) rigid body plates

After the simulation was completed, the sum of the reaction forces on the top surface nodes was plotted against the displacement of the same elements to determine the apparent stiffness. The calculated stiffness and the computing time were compared for each of the models in Figure 6.18. Each of the models produced perfectly linear deformation curves, with the coarsest mesh producing the stiffest gradient which was to be expected since it possessed the fewest nodes and degrees of freedom. The gradients showed convergence towards the most refined mesh with a 6% difference in the stiffness between the two most refined meshes, though it should be noted that there was an 80% increase in the amount of elements and a 300% increase in the computing time. These results indicated that the level of mesh refinement, and thus computing time, could be reduced without sacrificing much accuracy in the results.

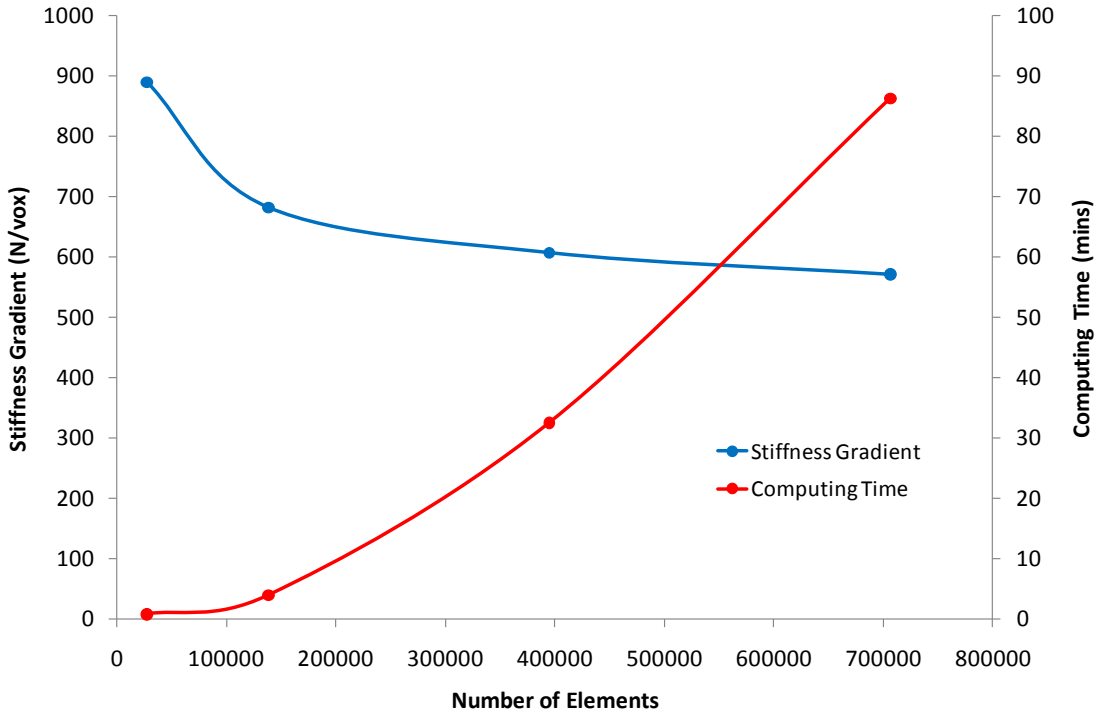

Figure 6.18 The variation of the stiffness gradient and the computing time as the mesh refinement is increased

6.3.3. Rigid Plate Compression

The next models were intended to make the simulations more realistic and thus two rigid bodies were created at both ends of the model to act as compression plates as shown in Figure 6.17b. The top plate was given a displacement in the z-axis while the other plate remained stationary. As a boundary condition for the model itself, the four bottom corner nodes were restrained in the x and y-axes to prevent any numerical instability. If these nodes were not restrained, the wafer model would undergo rigid body movement. A 'surface-to-surface' contact was used between each plate and the surface elements of the skins. The load-displacement graphs for the compression simulations with plates were compared to the previous graphs in which the surface elements were displaced in Figure 6.19.

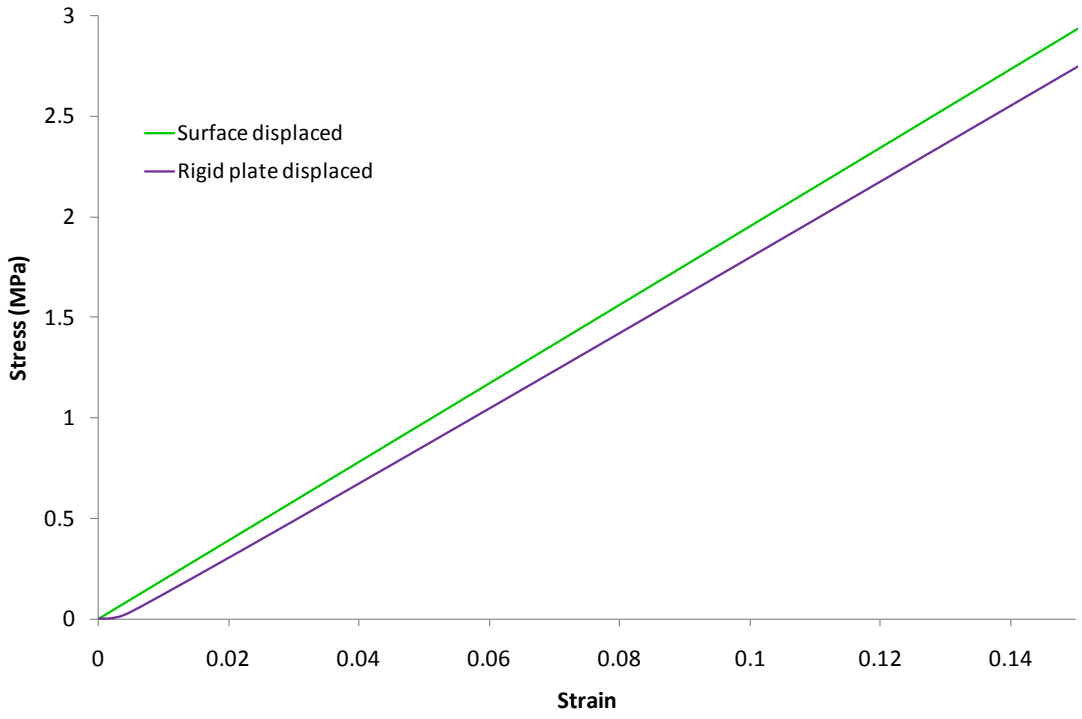

Figure 6.19 Load-displacement response of a model compressed with rigid plates and the top surface displaced

They both had almost identical gradients however the plate models produced graphs with an initial non-linear region which was reminiscent of what was observed experimentally. The cause of this initial non-linearity was attributed to either the internal cellular structure or the

asperities on the surface of the wafer [91]. This was investigated numerically using two specially created finite element models which are shown in Figure 6.20.

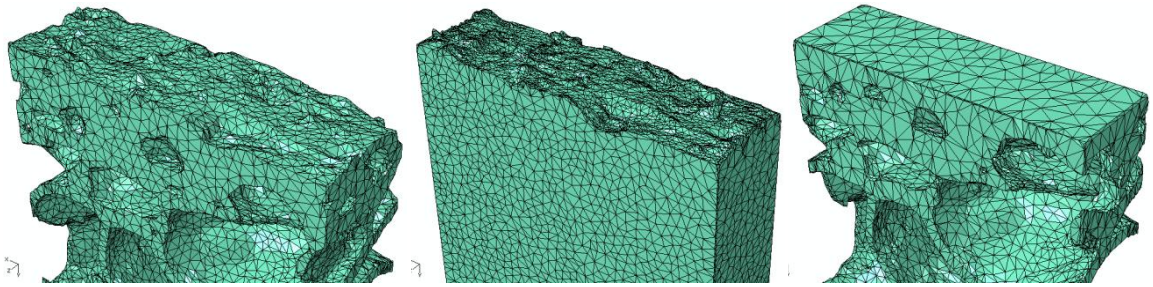

Figure 6.20 a) Original architecture, b) no cell walls, c) flat surfaces

A small section of the wafer was modified so that the surfaces of the skin region were perfectly flat as compared to the natural undulating surface. The second model was altered such that all the pores were filled with solid elements while the surfaces of the skin remained rough. Both of the models were compressed with rigid body plates and the resulting deformation curves were plotted in Figure 6.21 for comparison. The flat wafer produced a perfectly linear elastic load-deflection plot while the solid model deformed in an initial non-linear manner followed by linear compression. These results proved that the initial non-linearity in the compression curves was due to the rough surface of the wafer and not the cellular nature of its microstructure.

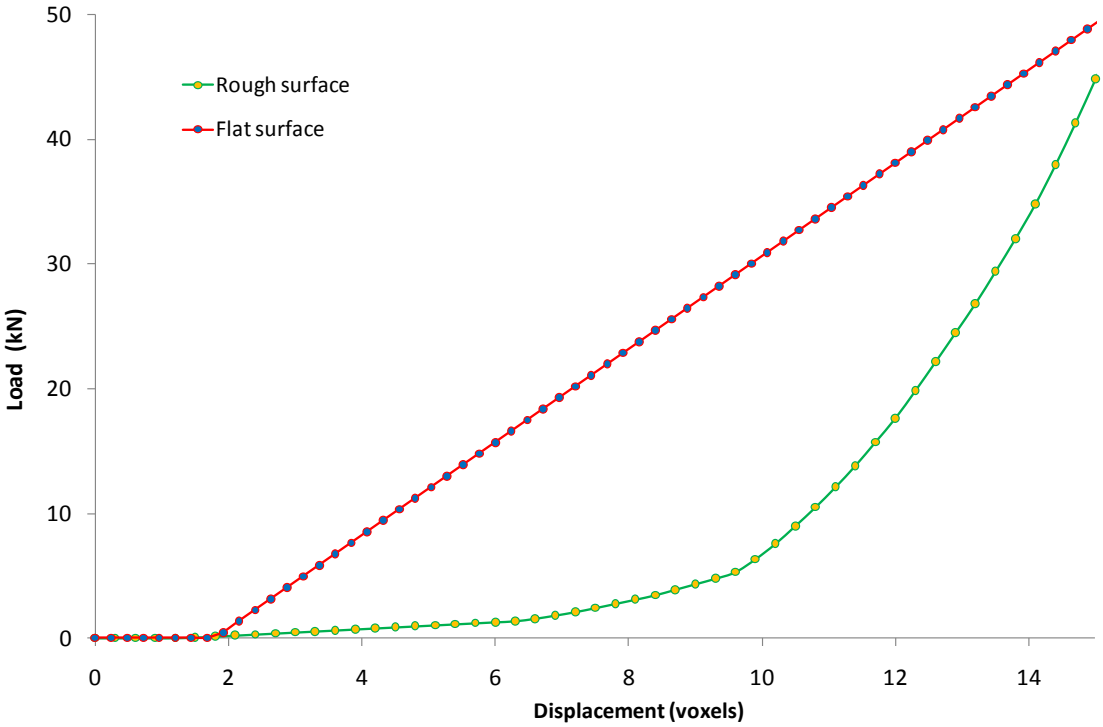

Figure 6.21 deformation curves of the models without cells walls and flat surfaces

6.3.4. Influence of the Wafer Core

Experimentally it was desirable to perform experiments on the skin and core regions separately. Preparing such samples however was challenging and hence not possible. However, tests on the skin or the core could be done virtually using the 3D volume obtained from X-ray tomography. The simple model used in the previous section was cropped, removing the skins and leaving only the core as seen in Figure 6.22.

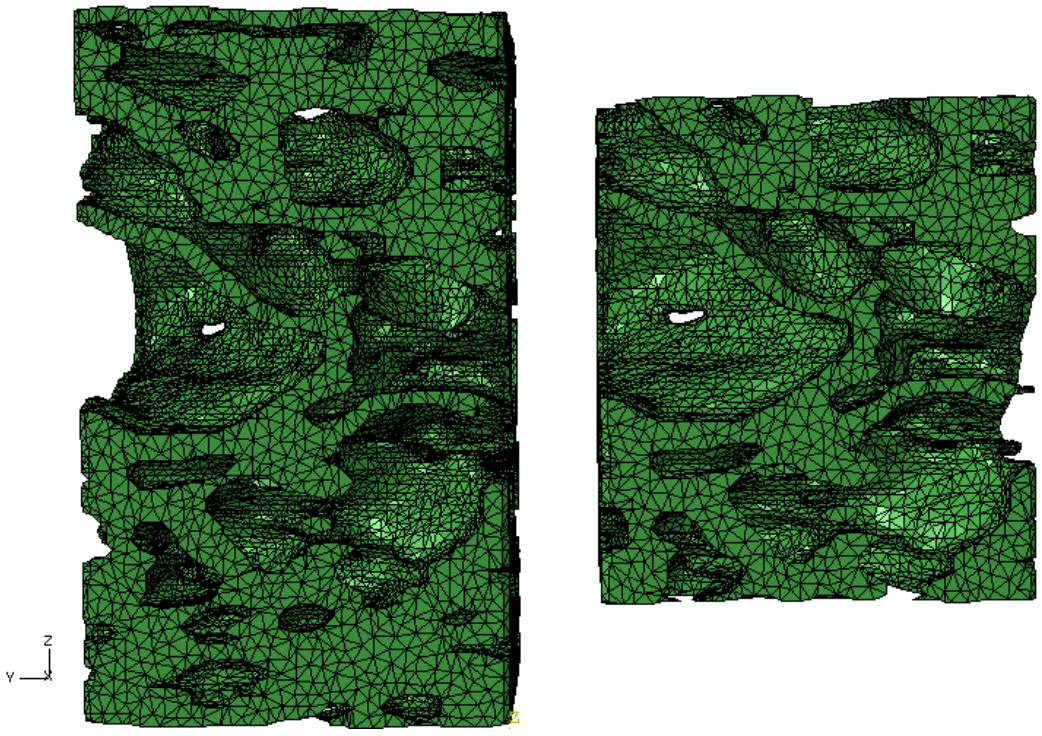

Figure 6.22 Initial model and cropped model of the core only

This model was compressed between two rigid plates and given the same boundary conditions as the skin and core model. The load-displacement output from the model was compared to the skin-core model to determine how much the core influences the overall deformation of the wafer in compression. The gradients of both graphs were used to determine the overall stiffness. The gradients were not identical but were quite similar which showed that while the core was significant in the compressive deformation, the skins did have a small effect as well. The gradient of the core stress-strain curve was used to obtain the apparent compressive modulus of the core which was then compared with the value calculated analytically in Section 5.3.3. This value was found to be 4 MPa which was the same order of magnitude as the analytical calculation, but a few times larger. This was most likely since the FE model represented approximately 1 x 1 mm instead of the RVE dimension.

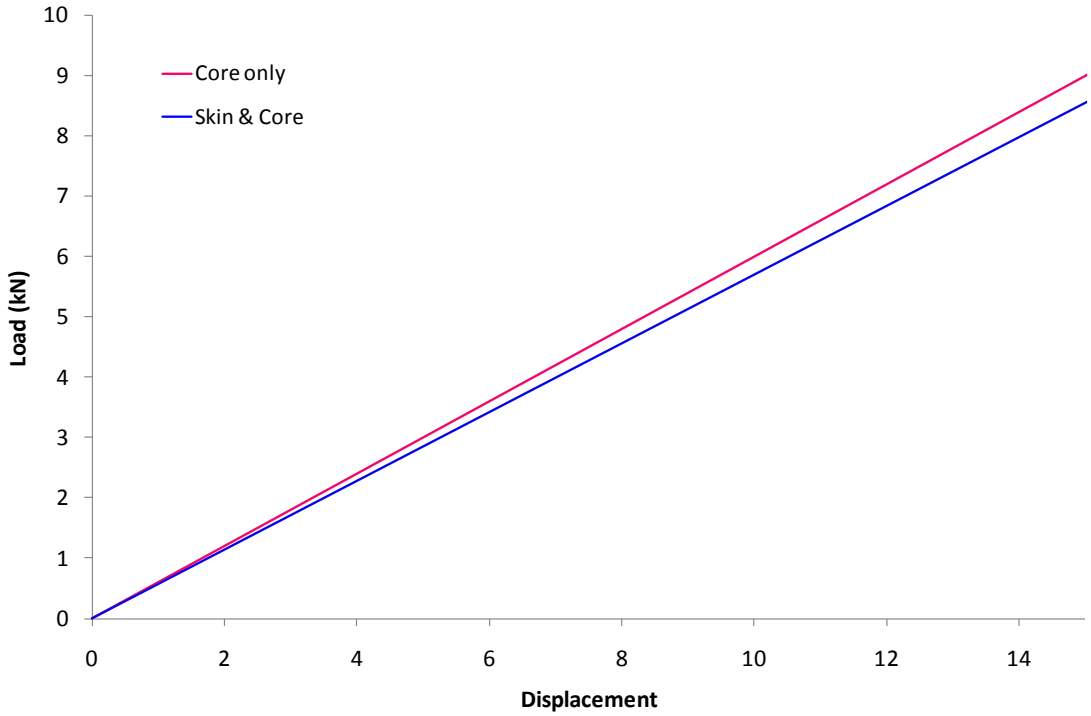

Figure 6.23 The deformation graphs of the skin-core model and the core only model

6.3.5. Comparison of Damage Models

It was desired to model the deformation of the wafer beyond the linear elastic region. The wafer was a brittle material and thus it would be necessary to simulate the fracture of the cell walls. This could be achieved using a damage function with an element deletion technique. Several damage options were available with the finite element software and they were all investigated before selecting the one which was most suitable for the wafer model.

The cohesive zone model [82] relies on the assumption that damage mechanisms leading to fracture are localized in a thin layer of material ahead of the crack tip. Cohesive elements are typically used to model adhesive joints and interfaces in composites. The failure zone is characterised by the stress (σ) and the separation (δ) within the zone which is referred to as the cohesive law or the traction separation law. As the loading increases, so too does the stress until a certain point at which damage initiation occurs (σ_c). As the damage grows, the stress decreases either linearly or exponentially, and vanishes at a certain critical separation (δ_c). The cohesive law is represented schematically in Figure 6.24.

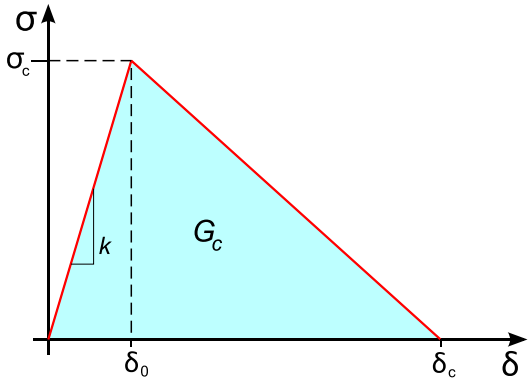

Figure 6.24 Graphical representation of the traction separation law

The area under the graph is equal to the critical strain energy (G_c) or the fracture energy. The stiffness slope (k) and energy parameters can be varied to represent the fracture within the cohesive zone. However there are limitations in using this damage model. The cohesive zone must be discretised with a single layer of elements through the thickness. As a consequence, it must be known in advance where the fracture in a model will occur in order to determine where to place the cohesive elements. Therefore the cohesive zone model could not be used for the wafer since it was impractical to assign all elements as cohesive and impossible to predict where fracture would occur within the complex architecture of the wafer. Another drawback of the cohesive elements is that its damage capability is active in tension only.

The concrete smeared cracking damage model [82] seemed like a viable option for the wafer since it was based on brittle fracture concepts. The model is typically used to define the properties of plain concrete beyond the elastic range. Abaqus offered three constitutive models, each of which was capable of modelling concrete and similar quasi-static brittle materials in various structures. One of these constitutive models, known as the brittle cracking model, is intended for applications in which the concrete behaviour is dominated by tensile cracking and the compressive failure in unimportant. The effective use of the brittle failure criterion relies on the user having some knowledge of the structural behaviour and potential failure mechanism. The fact that the brittle material loses its ability to carry tensile stress does not preclude it from withstanding compressive stress. In compression, the

material behaves elastically with no damage. As a result, this material model was not suitable for modelling the wafer.

The extended finite element method (XFEM) [82, 114] is an extension of the conventional finite element method which is available on the latest version of Abaqus Standard. It is an attractive way to simulate the initiation and propagation of a crack along an arbitrary, solution-dependent path without the need to remesh the model. When using XFEM, the first requirement is to define the crack domain which is the region which contains existing cracks and where these cracks may propagate. The position of the initial crack location does not necessarily need to be defined because Abaqus will create cracks during the simulation at positions which are experiencing stresses/strains which exceed the specified damage value. The damage initiation is based on either a maximum principal stress or strain and then followed by a user-defined evolution law. It is also possible to implement XFEM based on traction-separation cohesive behaviour. Unlike cohesive elements, the traction-separation behaviour in XFEM is confined to only the damage evolution. The advantage of XFEM-based segments over standard cohesive elements is that the crack path does not need to be predefined. As the crack is propagated through an element, it is cut into two parts due to the presence of 'phantom nodes'. When the element is cut, the potential compressive behaviour is taken into account by contact interaction properties between the split surfaces. XFEM appeared to be the ideal damage model for simulating the fracture of the wafer and was implemented in the trial wafer architecture model of Section 6.3.2. Elements within specific cell walls did fracture as seen in Figure 6.25. However the simulation kept aborting prematurely since only one crack could develop in the crack domain, which in this case was the entire wafer. It was impractical to specify multiple domains and further modelling with XFEM was abandoned.

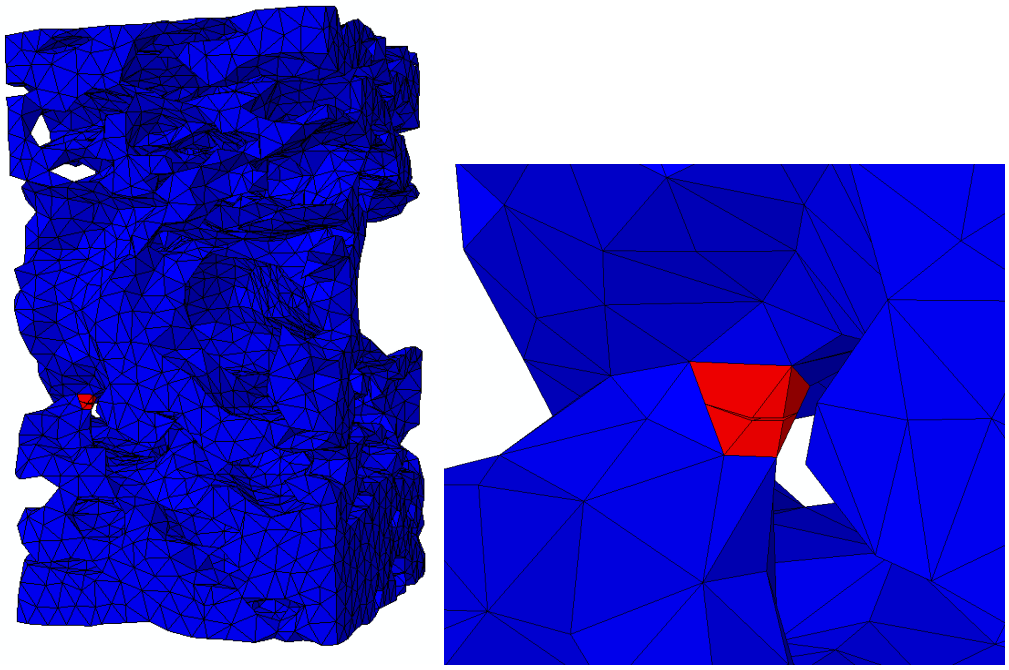

Figure 6.25 The damaged model using XFEM with a zoomed in region of the crack produced

The final damage model investigated was the ductile damage for metals material model. Despite the fact that the wafer was neither metal nor ductile, this model showed the greatest potential and is described in detail in the next section.

6.3.6. Ductile Damage for Metals Material Model

The ductile damage for metals material model on Abaqus was implemented to simulate damage of the cell walls of the wafer. This progressive damage model worked in conjunction with the elastic and plastic material models. The stress-strain curve of an element using this material model could be divided into three parts as represented on Figure 6.26. The linear elastic region is described by a-b, the plastic region by b-c and the evolution of degradation between c-d. The yield stress is at point b, the damage initiation criterion occurs at point c and the element deletes at point d. Element deletion means that the stiffness of the said elements has fully degraded to 0 and are thus no longer used in the finite element calculations.

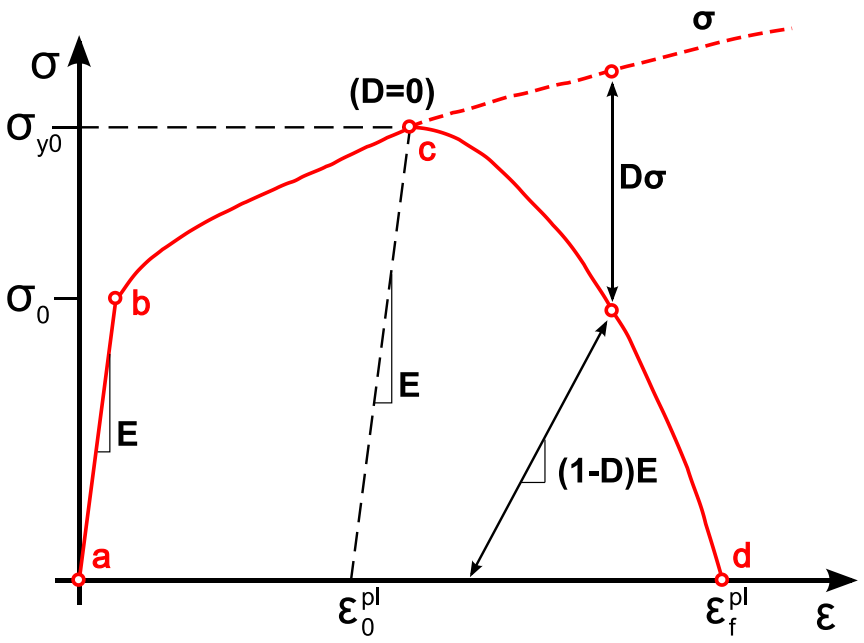

Figure 6.26 The stress vs strain response of the ductile damage material model

The damage evolution law described the rate of the material stiffness degradation of the elements when the damage initiation criterion had been reached. At any given time in the analysis, the material stress tensor is given by Equation 6.1. The undamaged stress tensor is σ_{un} which would exist in the absence of damage and D is the overall damage variable. Thus D=0 at pre-damage initiation and D=1 at element deletion.

$$\sigma = (1 - D)\sigma_{un} \tag{6.1}$$

The parameters for the elastic material model were the elastic modulus (E) and the Poisson's ratio (v). The yield stress (σ_{y0}) was the parameter for the plastic material model. The damage initiation was onset by an equivalent plastic fracture strain ($\varepsilon^{pl}{}_0$) while the damage evolution was determined either by a fracture energy dissipation (G_f) or a fracture plastic displacement ($u^{pl}{}_f$). The fracture energy per unit area is described by Equation 6.2.

$$G_f = \int_{\varepsilon_0^{pl}}^{\varepsilon_f^{pl}} L^{el}\sigma_y d\varepsilon^{pl} = \int_0^{u_f^{pl}} \sigma_y du^{pl} \tag{6.2}$$

The introduction of the characteristic element length (L^{el}) reduces the mesh dependency of the damage model and thus the damage evolution is characterised by a stress-displacement response. The G_f corresponds to the area under the stress-displacement graph during the damage evolution stage. The fracture displacement corresponded to the element displacement between the damage initiation and the element deletion. The damage evolution law can be specified in terms of either the fracture energy dissipation or the fracture plastic displacement. In the case of a linear evolution, the energy (G_f) and displacement at failure ($u^{pl}{}_f$) are related by Equation 6.3. Figure 6.27a graphically describes the fracture energy while Figure 6.27b shows the variation in the damage variable as an element is deformed until failure.

$$u_f^{pl} - u_0^{pl} = \frac{2G_f}{\sigma_{y0}} \tag{6.3}$$

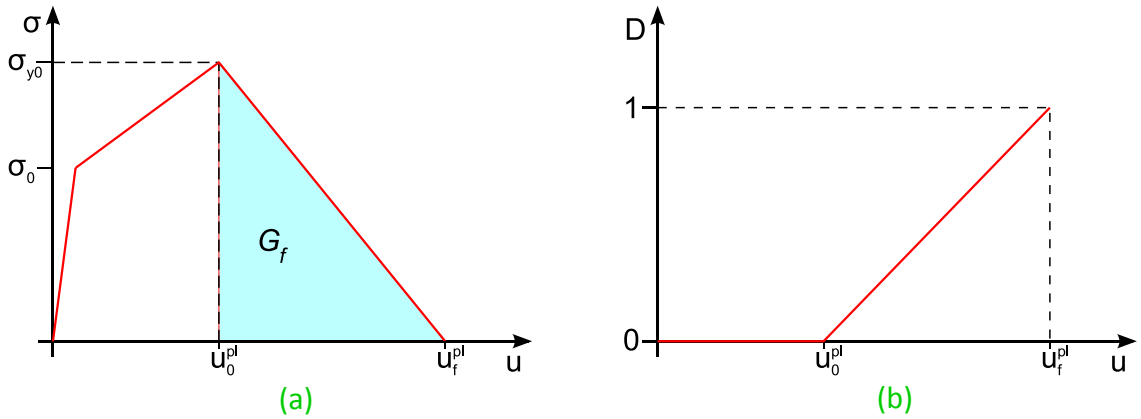

Figure 6.27 The a) graphical representation of the fracture energy and b) the damage variable evolution

It was assumed that the deformation curve parameters could be modified to simulate brittle fracture if there was no plastic region and the damage evolution was a steep, almost vertical line which is why this material model was selected for the wafer.

A single three dimensional element of unit dimensions was modelled with symmetrical boundary conditions on three faces and uni-axial displacement applied to the top face as shown in Figure 6.28. The input parameters of the model were varied sequentially in order to

fully understand the response of the ductile damage for metals material model. These parameters included the plastic fracture strain, fracture energy and damage degradation factor.

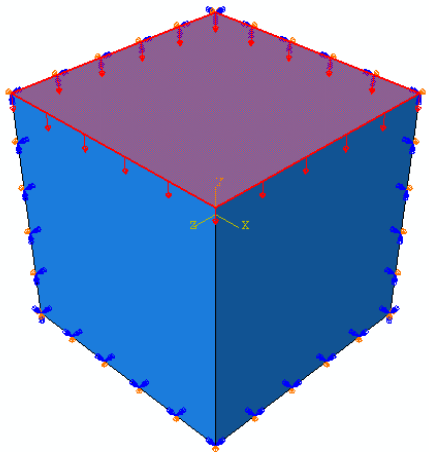

Figure 6.28 Boundary conditions of a single element model with ductile damage

6.3.7. Parametric Analysis of the Ductile Damage Material Model

An elastic modulus (E) of 150 MPa and Poisson's ratio (v) of 0 were input for the elastic material while a yield stress (σ_{y0}) of 25 MPa was given for the plastic material. An initial value of 0.1 was given for the fracture strain (ε^{pl}_{0}) and 1 for the fracture energy (G_f). Two other separate simulations were run using only the elastic and elastic-plastic material properties as a control to compare against the model with damage. The stress and strain output from each simulation was plotted and compared in Figure 6.29. The elastic model output a linear graph with a gradient equal to the input modulus. The elastic-plastic model produced a perfectly plastic response in that the stress-strain curve was linear until the input yield stress and then a horizontal line for all strains beyond this point. The damage model produced an initial linear elastic region and then a horizontal plastic region followed by a curve which degraded linearly until the stress was zero. The total plastic strain of the horizontal region was equal to the input fracture strain (ε^{pl}_{0}). A stress-displacement graph was also plotted and the area under the evolution section was calculated. This value was equal to the input fracture energy (G_f). The evolution displacement at failure (u^{pl}_{f}) could be measured from the graph and calculated using Equation (6.3 and in both cases the value was the same.

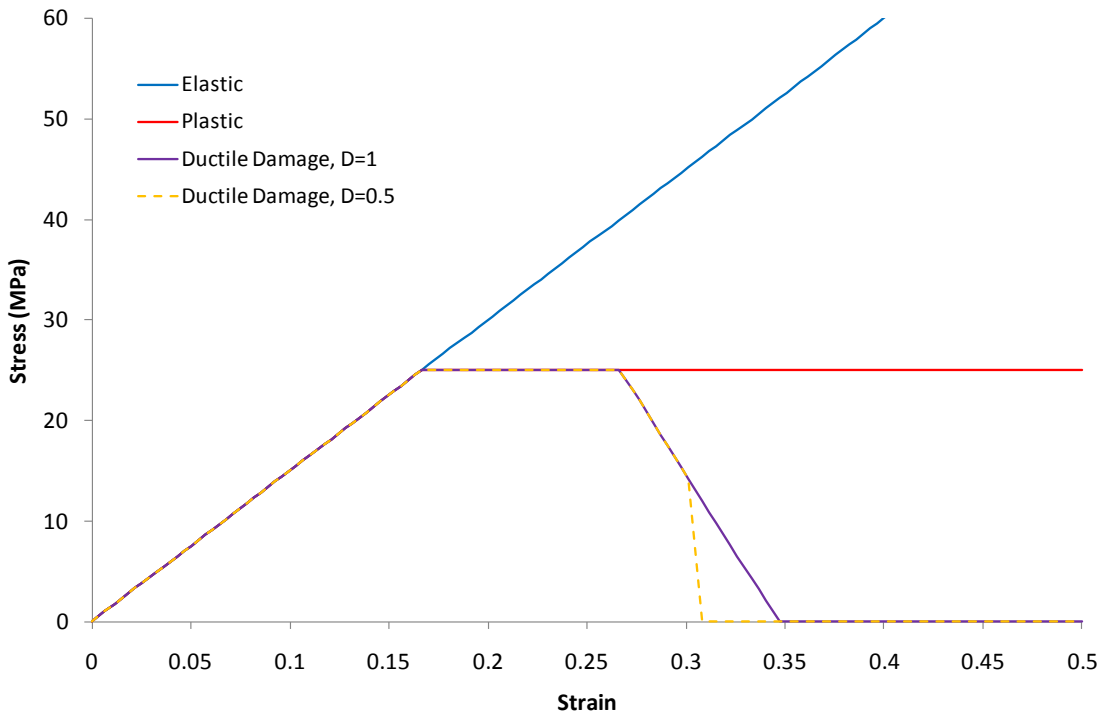

Figure 6.29 Comparison of the response of an element with elastic, plastic and ductile damage material model

By default, elements were deleted when the damage variable, *D*, was 1. However, this value could be reduced by changing the maximum degradation factor which then caused the element to delete at the specified factor along the natural damage evolution path. At this point, the deformation curve produced a near vertical evolution path as shown by the yellow line in Figure 6.29. The damage model was run several times, varying the value of the fracture energy while keeping all the other material constants the same. The gradient of the evolution was steeper as the energy was decreased with an almost vertical line when the fracture energy was set to zero as seen in Figure 6.30. The fracture strain was also varied while all the material properties including the fracture energy was kept constant as seen in Figure 6.31. As this value was decreased, the range of the plastic response was likewise reduced. However, Abaqus would not allow a fracture strain of exactly zero. The stress-strain responses as the fracture energy and fracture strain are varied are plotted in Figure 6.30 and Figure 6.31.

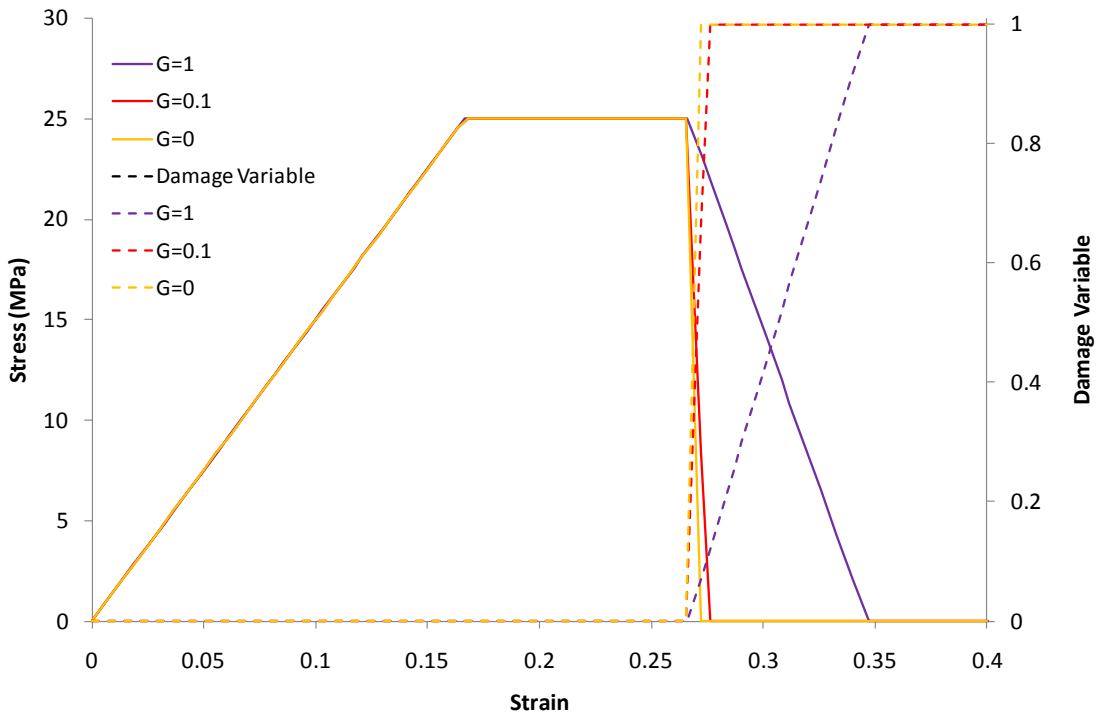

Figure 6.30 Effect of fracture energy (G_f) on stress-strain and D with fixed fracture strain (ε^{pl}_0) of 0.1

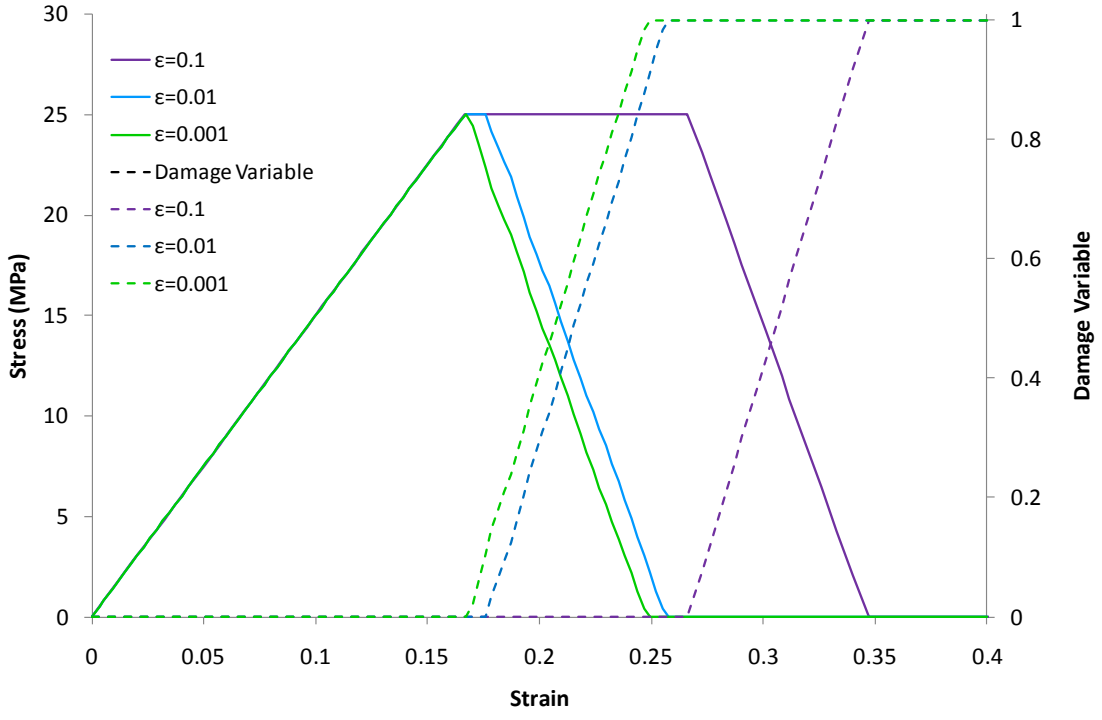

Figure 6.31 Effect of fracture strain (ε^{pl}_0) on stress-strain and D with fixed fracture energy (G_f) of 1

These results implied that if a very small fracture strain and zero fracture energy were input the resulting deformation would be linear elastic followed by almost instantaneous deletion of the element thus simulating a brittle material model. Ultimately, the single element model was given the same elastic and plastic parameters of 150 MPa and 25 MPa for the Young's modulus and yield stress respectively. The fracture strain was reduced to 0.001 and the fracture energy was set to zero. The deformation of the element is represented graphically in Figure 6.32 and shown to be a brittle response.

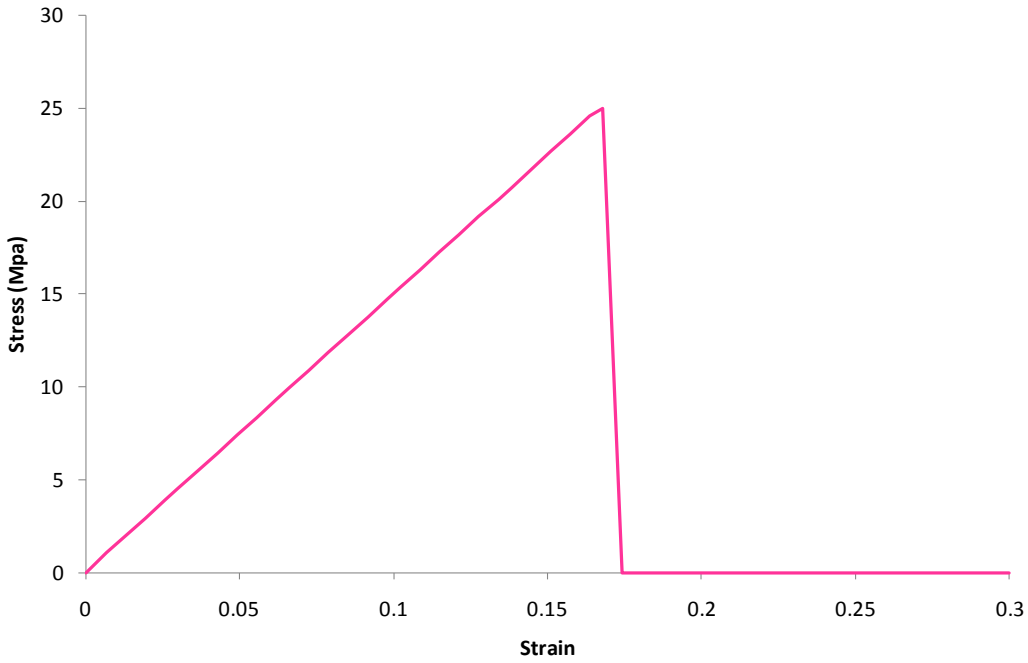

Figure 6.32 The ductile damage material model with brittle behaviour

6.3.8. Mesh Sensitivity

A single 2D element with ductile damage was compressed and then further refined to determine the mesh dependency of the material model. Since the geometry of the model was a square, the number of elements along each edge was the same. The global stress was plotted against the displacement for each meshed model as seen in Figure 6.33.

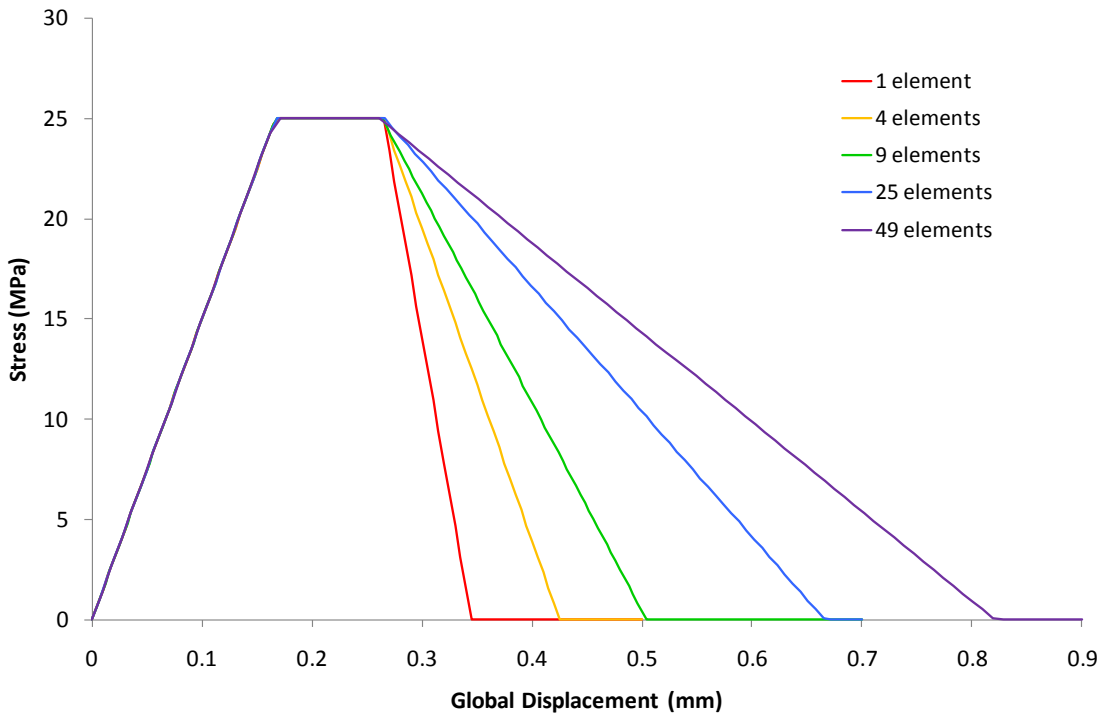

Figure 6.33 The effect of the damage evolution with mesh density

The results produced a trend in which the fracture displacement increased with the mesh density. The fracture displacement (u^{pl}_f), and thus the fracture energy (G_f), was shown to be proportional to the square root of the number of elements in Figure 6.34.

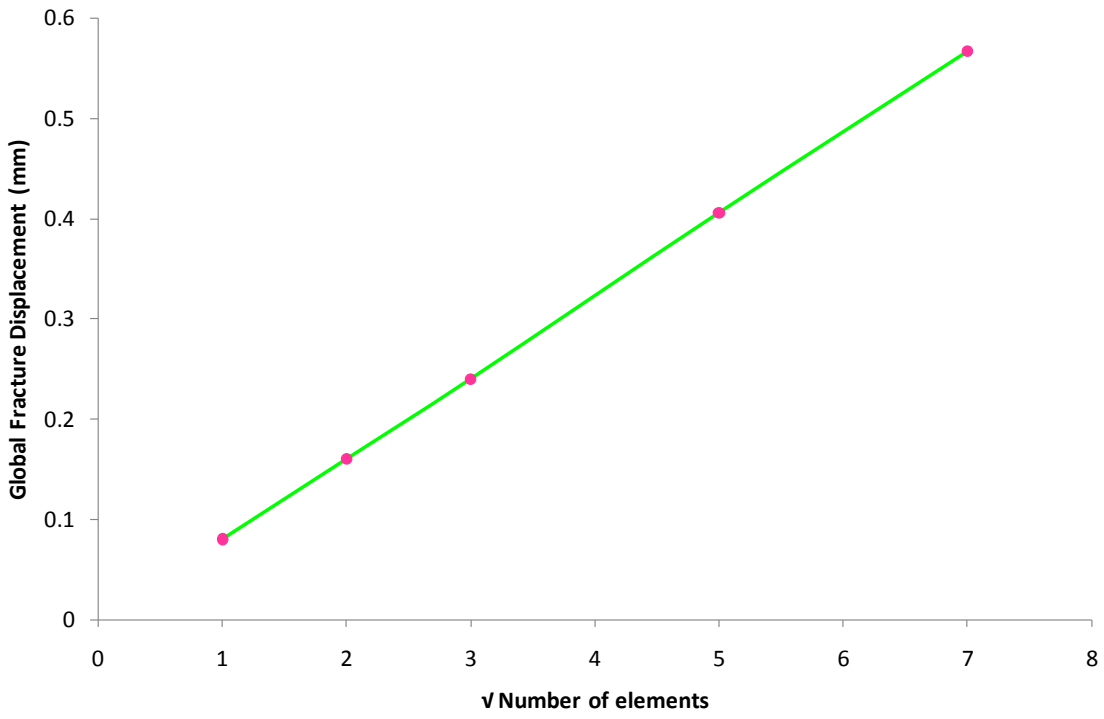

Figure 6.34 Relationship between the fracture displacement and the number of elements

This was consistent with Equation 6.2 in which the fracture displacement was directly proportional to the characteristic element length. This result also implied that for a 3D cube, the fracture energy would be proportional to the cubed root of the number of elements. The introduction of the characteristic element length is meant to make the solution mesh-independent, but this applies to models, such as tensile specimen with a hole, in which the stress concentration varies within different regions of the geometry. In these trial simulations with a square, the mesh density and stress was uniform, which explains why the results implied that the damage model was mesh-dependent. However, any mesh dependence of the damage model would be nullified due to the fact that a fracture energy of zero was being implemented to the model of the actual wafer architecture.

6.3.9. Abaqus Explicit

The ductile damage material model was next implemented into the wafer architecture compression simulations. However, they continuously aborted just beyond the elastic region,

regardless of what parameters were used in the material model. In an attempt to overcome this problem, the Abaqus Explicit solver was used instead [115].

Abaqus Standard uses an implicit solver which means that the state of the model at a specific time is calculated using data at that time. This involves using the iterative Newton-Raphson method which formulates a Jacobian stiffness matrix to enforce equilibrium in the model. For complex problems involving non-linear deformation or contact between surfaces, convergence can be very slow and the solution may even diverge. Abaqus Explicit was originally developed to solve dynamic problems but can be adapted for quasi-static situations. Unlike the implicit solver, the explicit solver calculates the state of the model at a specific time based on the results from the previous increment of time. Thus a large number of small time increments are needed in order to obtain an accurate solution. As a result, the model can become computationally demanding to solve. Abaqus Explicit does not require a stiffness matrix since it utilises a Euler integration scheme and, because no iterations are involved, convergence is not an issue. Since Abaqus Explicit is a dynamic solver, the density of the material needed to be included to account for inertial effects and the total step time needed to be varied using a trial and error approach in order to ensure a quasi-static simulation.

Before modelling the wafer architecture, a single element was displaced and the deformation output was calculated using the Explicit solver. As a control, the same single model was run on Abaqus Standard using the implicit solver. The time period or step time was the first parameter that was varied and it was shown that for small step times, the output was unstable due to dynamic instabilities. The results stabilised as the step time was increased and beyond a threshold time, the deformation curve was the same as the implicit solution and the analytical calculation. The density (ρ) of the material and the total time period (T) were related by Equation 6.4 where n was the number of increments required for the solution.

$$n = T\left[\max\left(\frac{1}{L^{el}}\sqrt{\frac{\lambda + 2\mu}{\rho}}\right)\right] \tag{6.4}$$

The characteristic element length was defined as L^{el} and the geometric Lamé constants were represented by λ and μ. The number of increments determined how computationally expensive the simulation will be. Reducing the total step time can introduce not only unwanted inertial forces but can also affect the result in the case of rate dependent materials. From the relationship in Equation 6.4, the same result could be obtained by artificially increasing the material density which is known as 'mass-scaling'. Thus, by carefully manipulating the step time and the density, the total runtime of the simulation could be reduced while still maintaining a quasi-static status. Mass scaling was applied to the wafer model by increasing the material density to 1 kg/mm^3 instead of using the measured value of 0.00112 g/mm^3 found in Section 4.2.1.

The wafer architecture model of Section 6.3.2 was again run, only this time using the Explicit solver. As before, the material model was linear elastic with no damage function or contact interaction between elements. The purpose of these simulations was to determine the step time which would produce the identical output from the implicit Standard solver. The deformation graphs are plotted in Figure 6.35 and show that the results converge to the Abaqus Standard solution as the step time is increased.

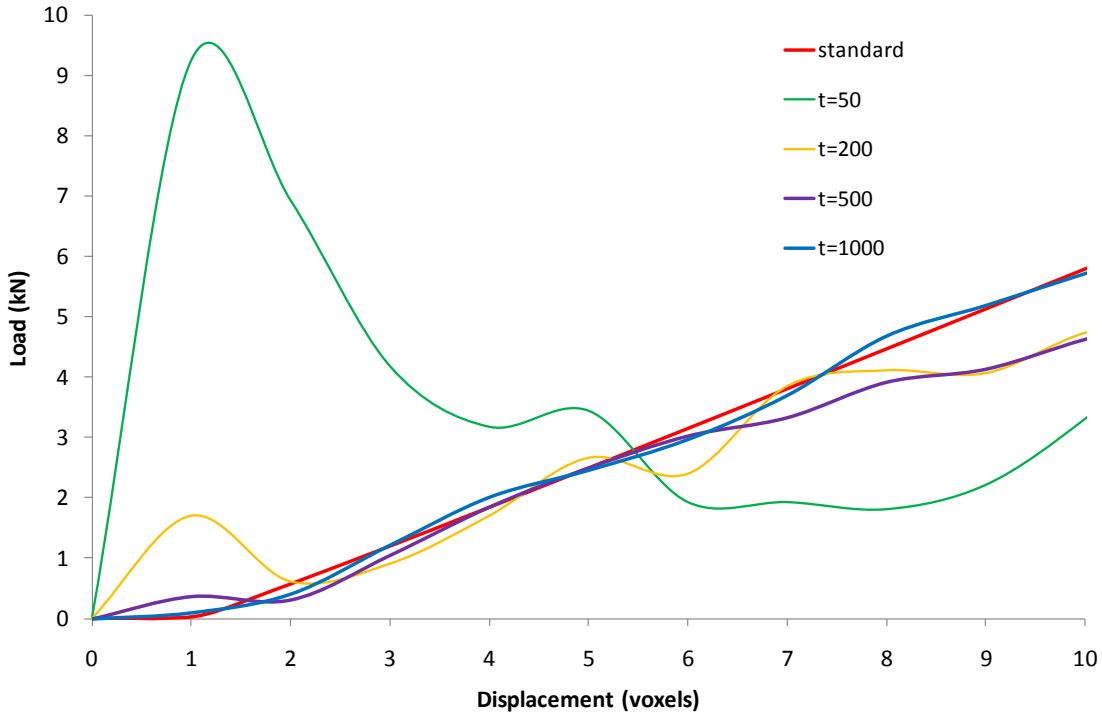

Figure 6.35 Load-displacement output for preliminary wafer model using Abaqus Explicit with varying step times

Once a suitable quasi-static step time was determined, the ductile damage material model was implemented. This time the simulation was fully completed and elements progressively deleted as the rigid plates compressed the model. The load-displacement output is plotted in Figure 6.36 and compared to the FE model at different stages of its deformation (Figure 6.37). The graph was initially linear followed by a jagged pattern reminiscent of a brittle foam. From the stress contour plots on the mesh, it could be seen that the stress concentrations developed within the core region where the cell walls were thinnest. The first element deletion occurred at these sites and continued to propagate at further stress concentrations. The non-linear section of the graph corresponded to elements being deleted and the remaining elements contacting each other. These results were quite promising, so the model was expanded to include a representative volume element of the wafer.

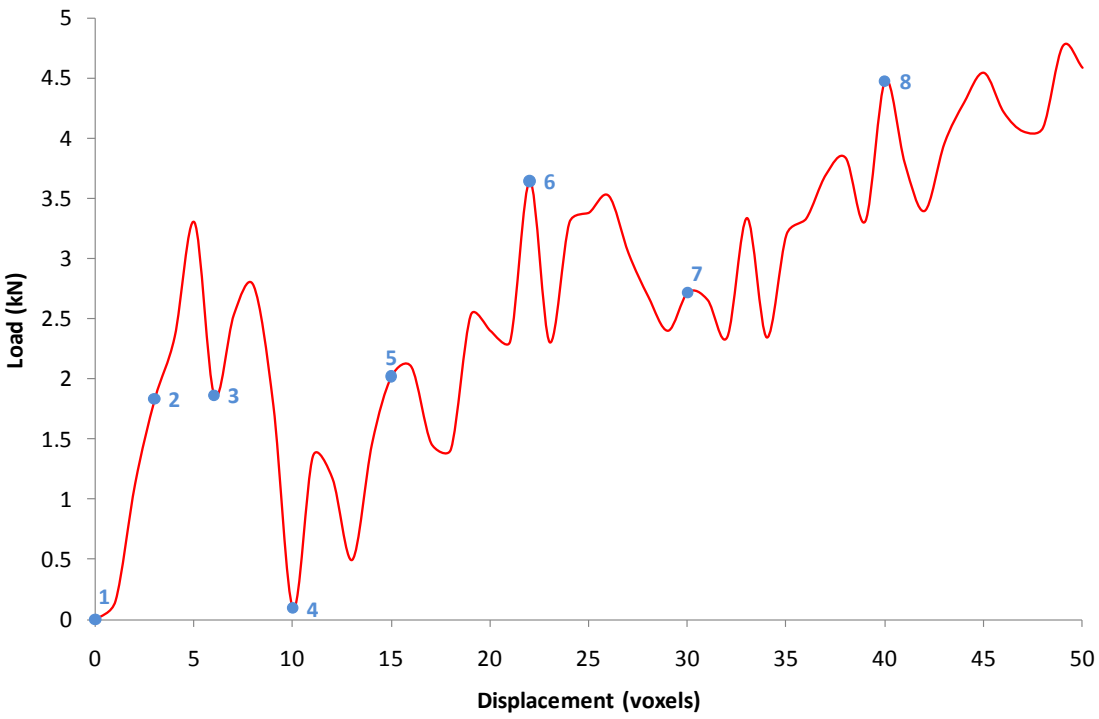

Figure 6.36 Load-displacement output of the preliminary compression model using the ductile damage material model

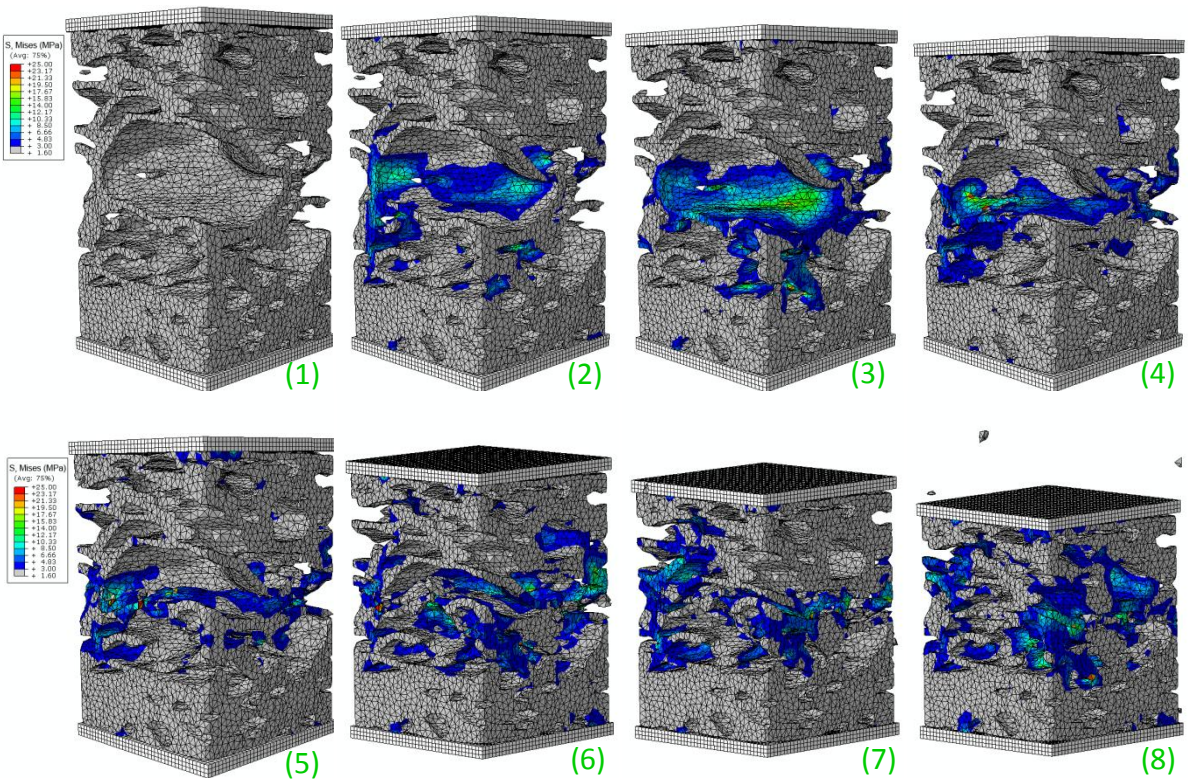

Figure 6.37 The damaged model at different stages in the compression

6.4. Finite Element Model of the Wafer RVE

6.4.1. Compression Simulation

The finite element calculations were intended to simulate the deformation of the wafer as observed in the compression experiments. The 3D generated mesh of the wafer architecture was imported into Abaqus as an orphan mesh (externally generated, non-modifiable mesh) as seen in Figure 6.38. The wafer model consisted of 60998 nodes and 230286 linear 4-noded tetrahedral elements (C3D4). This was the most refined mesh which could be generated using the maximum capability of the Avizo software. The dimensions of the model was scaled to mm, as compared to voxels of the previous trial models, and was approximately 2.5 mm in both directions representing the RVE of the wafer. Two analytical rigid body parts were created above and below the wafer model to act as the compression plates.

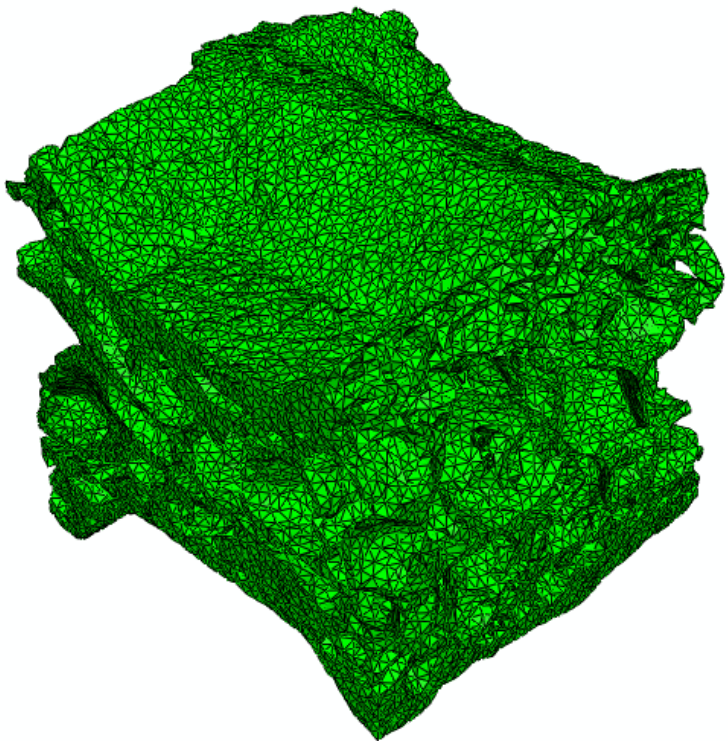

Figure 6.38 The finite element mesh of the RVE of the wafer with its actual architecture

For the boundary conditions, each rigid plate was displaced an equal and opposite amount in the y-axis. Abaqus Explicit was used for the compression simulations and thus an amplitude was required for the displacement of the rigid bodies. A linear amplitude was chosen as this gave the plates a uniform displacement and thus constant speed. The four vertical faces of the wafer were each given symmetry boundary conditions perpendicular to the plane of each face. The boundary and loading conditions are better visualised in Figure 6.39. Since the actual geometry of the mesh represented roughly 2.5mm of the wafer, applying symmetrical boundary conditions replicated a 7.5mm x 7.5mm wafer specimen. This dimension was significant because both the in-situ SEM and in-situ XMT compression tests were performed on specimens of this size.

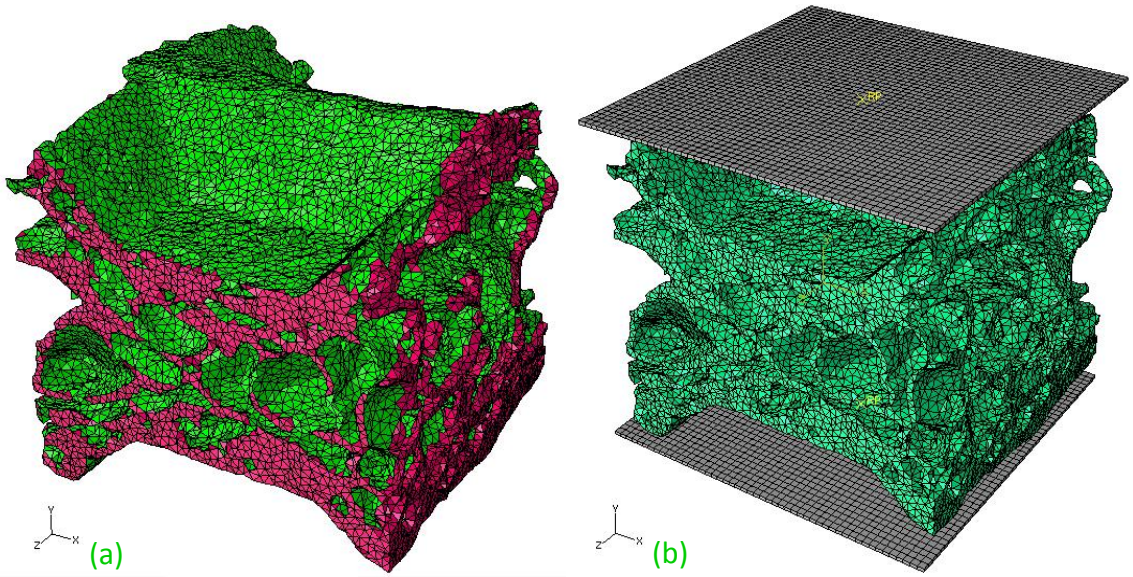

Figure 6.39 The a) symmetrical boundary conditions (pink elements) and b) rigid plates for loading

Beyond the elastic region of compression, there was contact between adjacent cell walls of the wafer and thus it was necessary to also include this in the finite element calculations. The 'surface-to-surface' interaction described contact between a rigid body (master) and a deformable body (slave) such as the compression plates and the wafer. The 'self-contact' interaction described contact between different areas on a single surface, as would be the case of collapsing cell walls in the wafer core. It would prevent inter-penetration between elements during the deformation. The drawbacks to self-contact were that the selected surface could not be discontinuous, the interacting regions would have to be known in advance and also selected manually which would be no simple task given the complex architecture of the wafer architecture. Therefore, 'general contact' was assigned to the entire assembly. This option allowed contact between the rigid plates and the wafer as well as self-contact between cell walls of the wafer model with a single interaction. General contact selected all exterior surfaces of the model, including analytical rigid surfaces, and was also capable of spanning unconnected regions of the model. The default interaction properties provided by Abaqus were used and consisted of normal and tangential behaviours which were 'hard-contact' and 'frictionless' respectively.

Abaqus Standard was initially used to model the wafer deformation. However, a combination of a complex architecture, a damage function and surface contact interactions resulted in convergence problems for the implicit solver. To overcome this problem, Abaqus Explicit was used instead since it uses a different solver which has a greater chance of converging. In order to simulate quasi-static conditions, a long enough step time was required in order to ensure that the dynamic effects were damped and the inertial effects were negligible. A consequence of this is that a large number of increments are required and thus the computing time required for a solution also increases. However it is possible to accelerate the solution time without compromising the solution accuracy by using a technique called 'mass scaling'. It enables an analysis to be performed without artificially decreasing the loading rate but by artificially increasing the density. To ensure that the simulation was producing a quasi-static response, the energy balance in the model should be analyzed and as a general rule the kinetic energy of the deformable body should not exceed 10% of its internal energy throughout most of the time history output.

The material properties of the wafer were the final parameters required for the model. The solid material of the wafer was assumed to be linear elastic. The elastic material model on Abaqus required a Young's modulus and Poisson's ratio for the input parameters. It was desirable to predict the material response beyond the linear elastic region and thus element deletion was used to simulate the fracture of the cell walls. The damage function implemented for this was the ductile damage for metals material model which was described in Section 6.3.6.

6.4.2. Compression Simulation Results

It was important to confirm that the simulation did in fact represent quasi-static deformation. This was achieved by increasing the step time, while keeping all other parameters fixed, until convergence was observed with the resulting stress-strain graphs. Also, the ratio of the model's kinetic energy to internal energy was plotted against time in Figure 6.40. The step time was deemed suitable for a quasi-static analysis if the ratio was less than 10% for the majority of the simulation. Based on the results in Figure 6.40, all future simulations were run using this minimum suitable step time, which in this case was 20s.

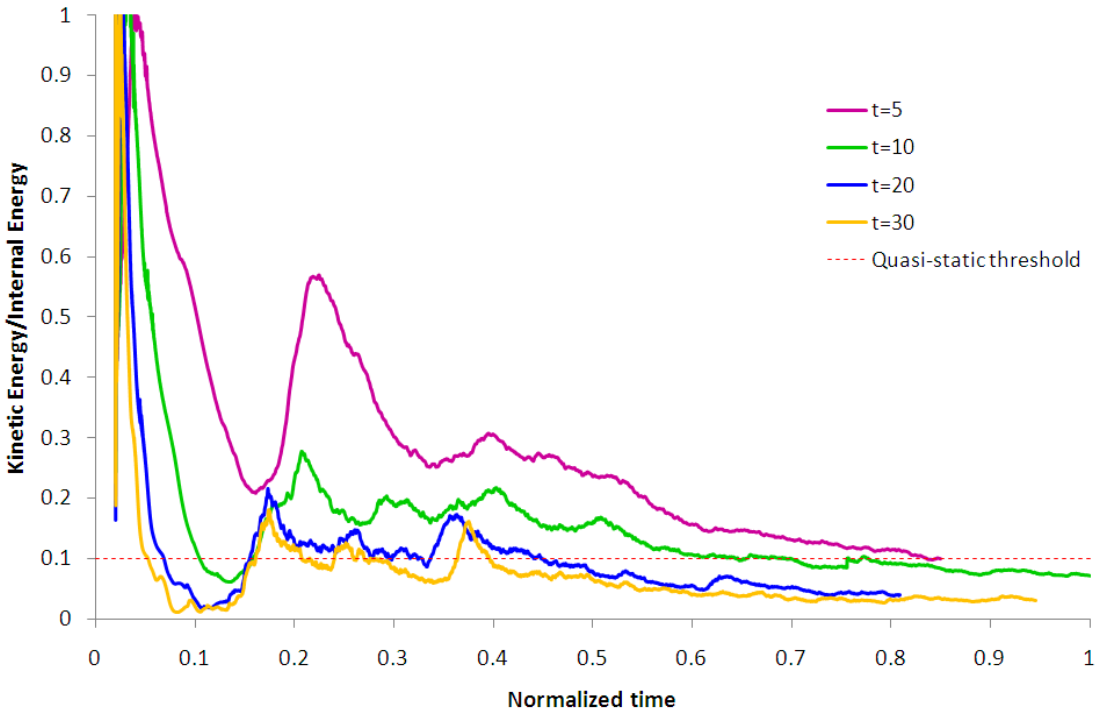

Figure 6.40 The KE/IE ratio for simulations with varying step times

The precise value of the wafer solid modulus was unknown and had to be estimated for the finite element model. The analytical calculations performed in Section 5.4 provided a range of possible values to be input for the solid modulus of the wafer material. The solid modulus was calculated using equations for cellular solids which related the foam and solid modulus to the foam relative density. The foam modulus was measured from the experimental compression data while the relative density was obtained from the XMT volumetric analysis. The estimated solid modulus of 200 MPa was used in the model and the output was compared to the experimental stress-strain curve in the elastic region. An inverse analysis was performed by varying the input Young's modulus and comparing the stress-strain output with the experimental curves as shown in Figure 6.41.

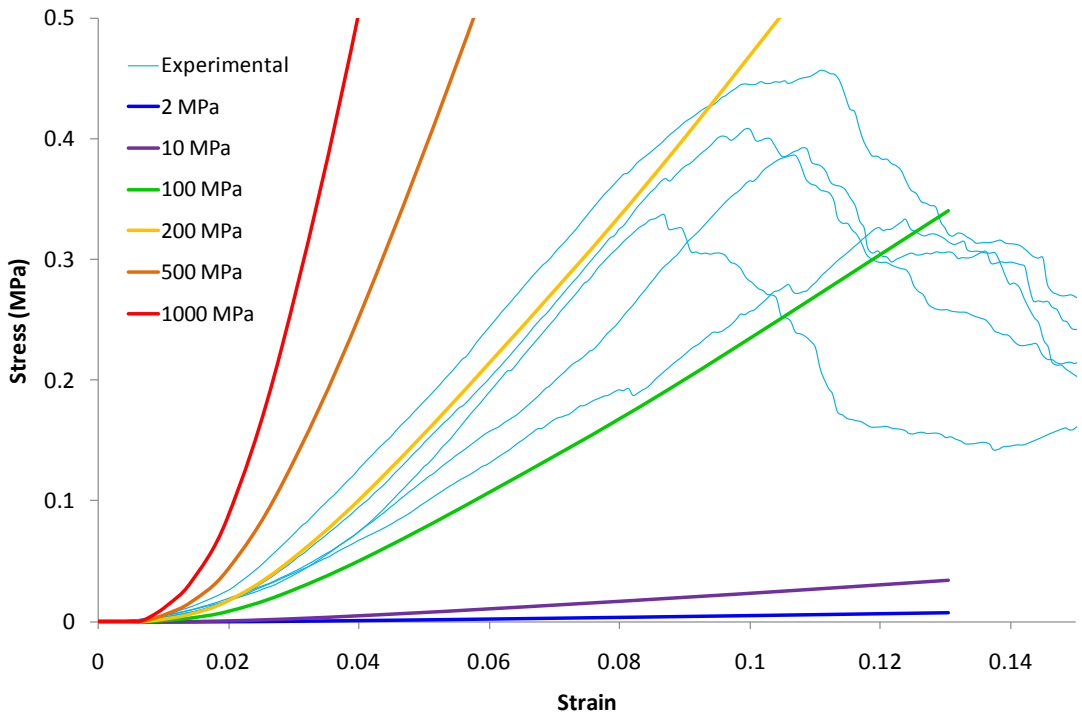

Figure 6.41 The effect of the solid Young's modulus on the deformation response of the model

Solid modulus values between 100 MPa and 200 MPa produced deformation curves which most closely followed the trend of the experimental plots. The foam modulus of the FE wafer model was determined using the gradient of the stress-strain plot and then a relative elastic modulus was calculated using the ratio of the foam modulus (E^*) and solid modulus (E_s). This ratio was compared to the predictions of the various analytical models described in Section 5.4 and the results are shown in Figure 6.42.

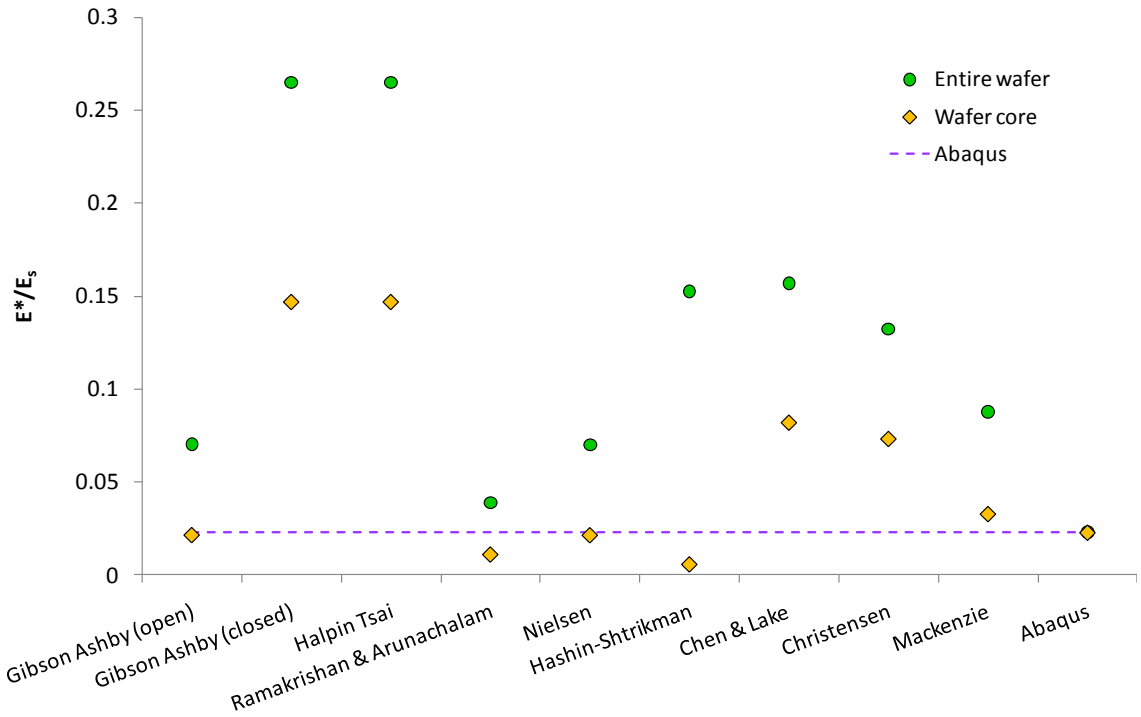

Figure 6.42 Comparison of the Abaqus FE output to various analytical foam models for E^*/E_s

The analytical calculations which used the relative density of the wafer core rather that the relative density of the entire wafer resulted in relative modulus values which were closer to the finite element prediction. Of note is the fact that the Gibson & Ashby prediction for fully closed celled foams is far from the finite element output while the opened celled equation was in good agreement. As discussed in Section 5.4.1, if the cells walls were thin then the minority of the solid material would be in the cell wall membranes and the relative foam modulus was closer to the analytical opened-cell foam model. Some of the other analytical models were also quite close to the FE output. The results validated the accuracy of the finite element model and the assumption that the relative density of the wafer core should be used to determine the solid modulus of the cell wall material. The calculated solid modulus value using each analytical model can be found in Table D1 of Appendix D.

The Poisson's ratio was an unknown material property, so a parametric study was performed with a fixed Young's modulus of 200 MPa and Poisson's ratio values ranging between 0 and 0.3. By performing these simulations it was possible to determine the solid modulus and

Poisson's ratio of the wafer which best fit with the experimental data. Only the elastic region of deformation was of interest, so the model was simplified to exclude the damage function and self-contact between cell walls. Figure 6.43 shows that the Poisson's ratio had minimal effect on the overall deformation.

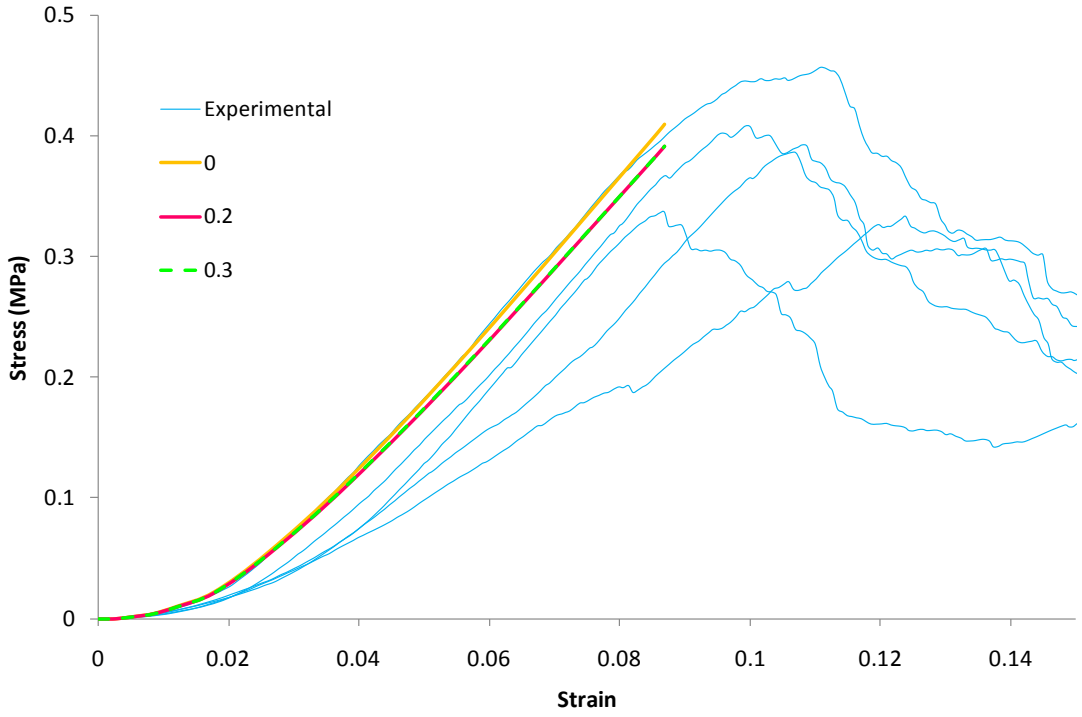

Figure 6.43 The effect of the Poisson's ratio on the deformation response of the model

The yield stress input required by Abaqus was the equivalent to the fracture stress of the cell wall material. The Young's modulus and Poisson's ratio values were kept constant at 200 MPa and 0.3 respectively. The damage criterion was implemented to this model using the parameters (ε^{pl}_{0} = 0.001 and G_f = 0) obtained in the single element analysis to simulate brittle fracture of the cell walls. The yield stress value was varied and the apparent stress-strain curves output from the Abaqus simulation were plotted and compared with the experimental graphs. Self contact between elements was not used for these models and as a result elements intersected each other as the compression progressed. However, because the damage criterion was present, elements deleted progressively to the point that there was no longer any resistance to the compressive displacement of the rigid plates. Graphically

this was represented by an initial linearly increasing stress followed by a progressive decrease until zero due to the deletion of elements. An input yield stress of 25 MPa, close to the analytical fracture stress of an opened cell foam of 31 MPa, produced an initial peak at the lower spectrum of the range of the experimental graphs. A yield stress of 50 MPa output a stress-strain plot that was closer to the upper bound of the experimental curves.

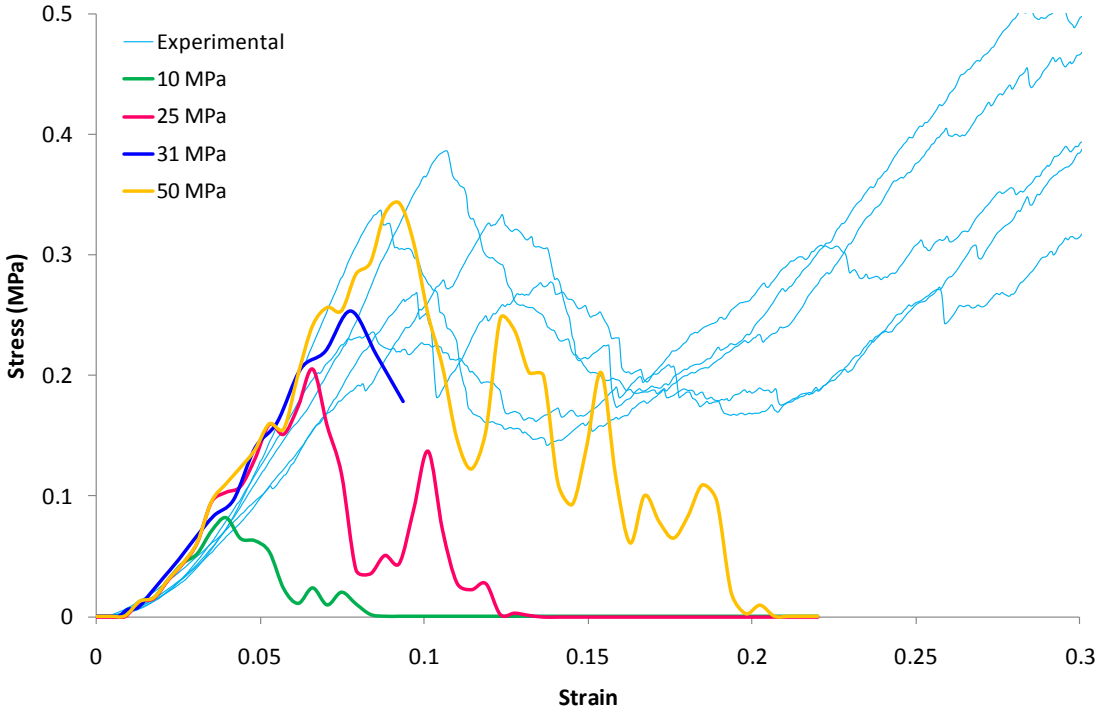

Figure 6.44 The effect of the solid yield stress on the deformation response of the model

Similar to the solid modulus, the relative fracture stress (σ^*/σ_y) could be estimated using the analytical Equation 5.17 which related the relative density of a foam to its rupture stress (σ^*) and the cell wall fracture stress (σ_y). The Gibson & Ashby analytical models [12] for open and closed-cell brittle foams were used for both entire wafer and the wafer core to obtain the relative fracture stress which was then compared to the output from the finite element model in Figure 6.45. For the finite element model, the rupture stress was the input yield stress value while the brittle collapse stress was the global stress of the wafer model at the point of initial fracture.

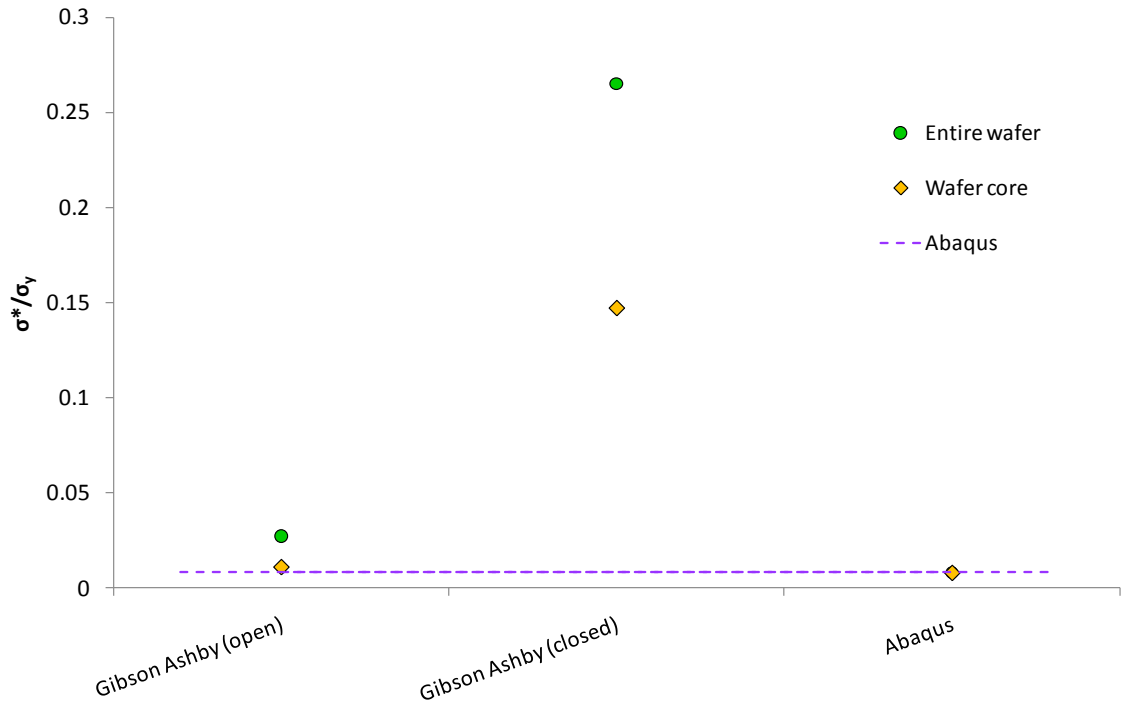

Figure 6.45 Comparison of the Abaqus FE output to various analytical foam models for σ^*/σ_y

The final consideration of the model was the potential contact between adjacent cell walls as the element deletion propagated. This was implemented using the general contact interaction described earlier. The material parameters which were used for the final model are listed in Table 6.1 and an abbreviated version of the Abaqus input file can be found in Appendix E.

Table 6.1 The numerical values of the material model parameters

Young's Modulus [E] (MPa)	Yield Stress [σ_{y0}] (MPa)	Poisson's Ratio [v]	Fracture Strain [ε^{pl}_0]	Fracture Energy [G_f] (kJ/m^2)
150	25	0.3	0.001	0

Graphically, the simulation produced a linear elastic region, then a sharp drop in the stress followed by a jagged region typical of a brittle foam with a rising trend in the stress as the strain increased. The contact between adjacent cell walls accounted for the jagged region. The output was plotted with the experimental stress-strain curves as a comparison. The

curves are seen in Figure 6.46 and show that the FE simulation underpredicted the stress at initial fracture but produced similar deformation trends in the plateau region as were observed experimentally.

Figure 6.46 The simulation output compared to experimental curves

Visually, elements were seen to be deleting and then as the wafer model was further compressed, the cell walls within the core region collapsed on each other. This was quite similar to the deformation that was observed from the in-situ SEM compression experiments. The stress contours on the wafer model showed that the initial stress concentrations occurred within the core of the wafer and thus it was the site at which element deletion initiated. Figure 6.47 to Figure 6.49 show a contour plot of the FE model at different stages of the compression. The images on the left and right represent a cross-section of the wafer RVE taken from the zy-plane and xy-plane respectively.

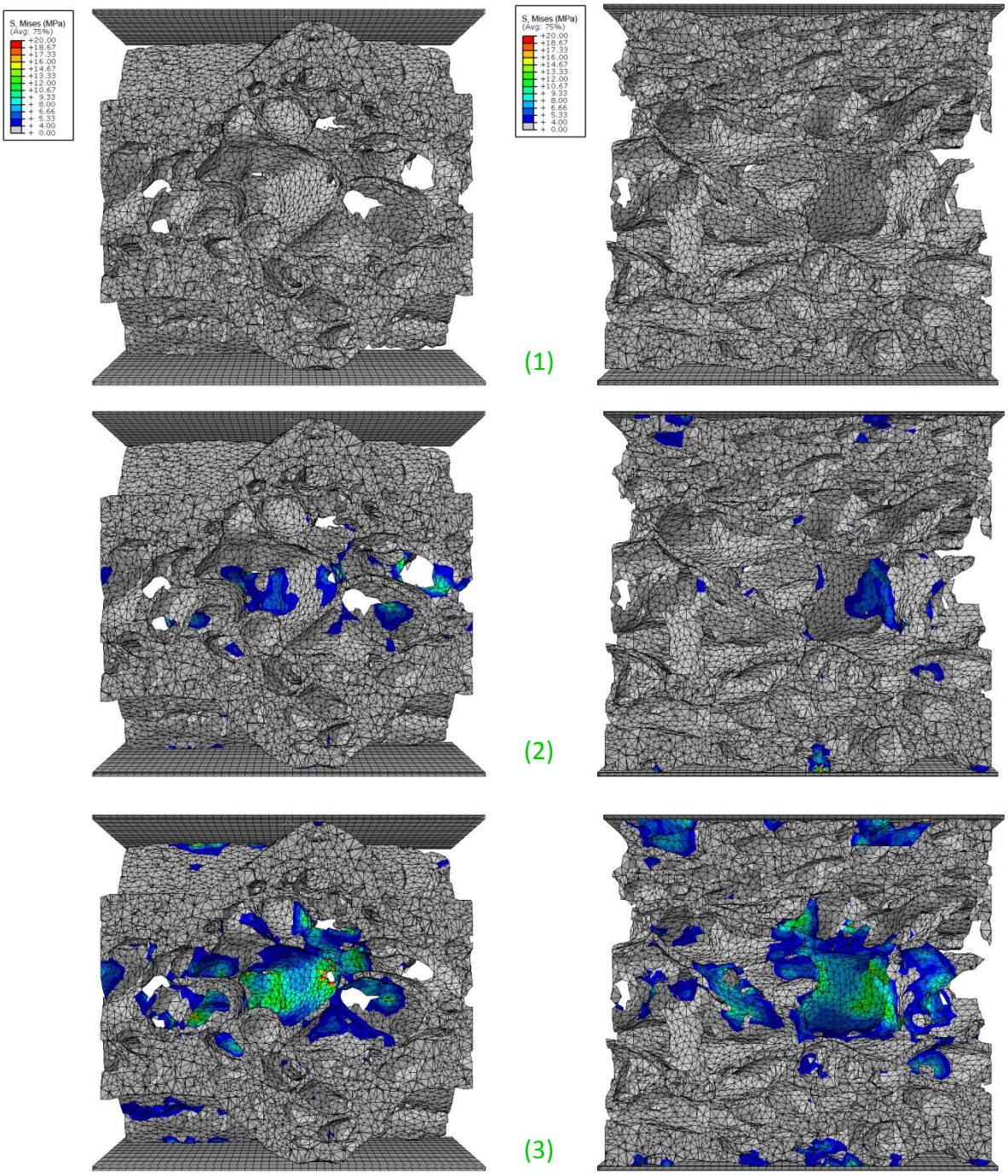

Figure 6.47 The damaged wafer RVE at different stages in the compression

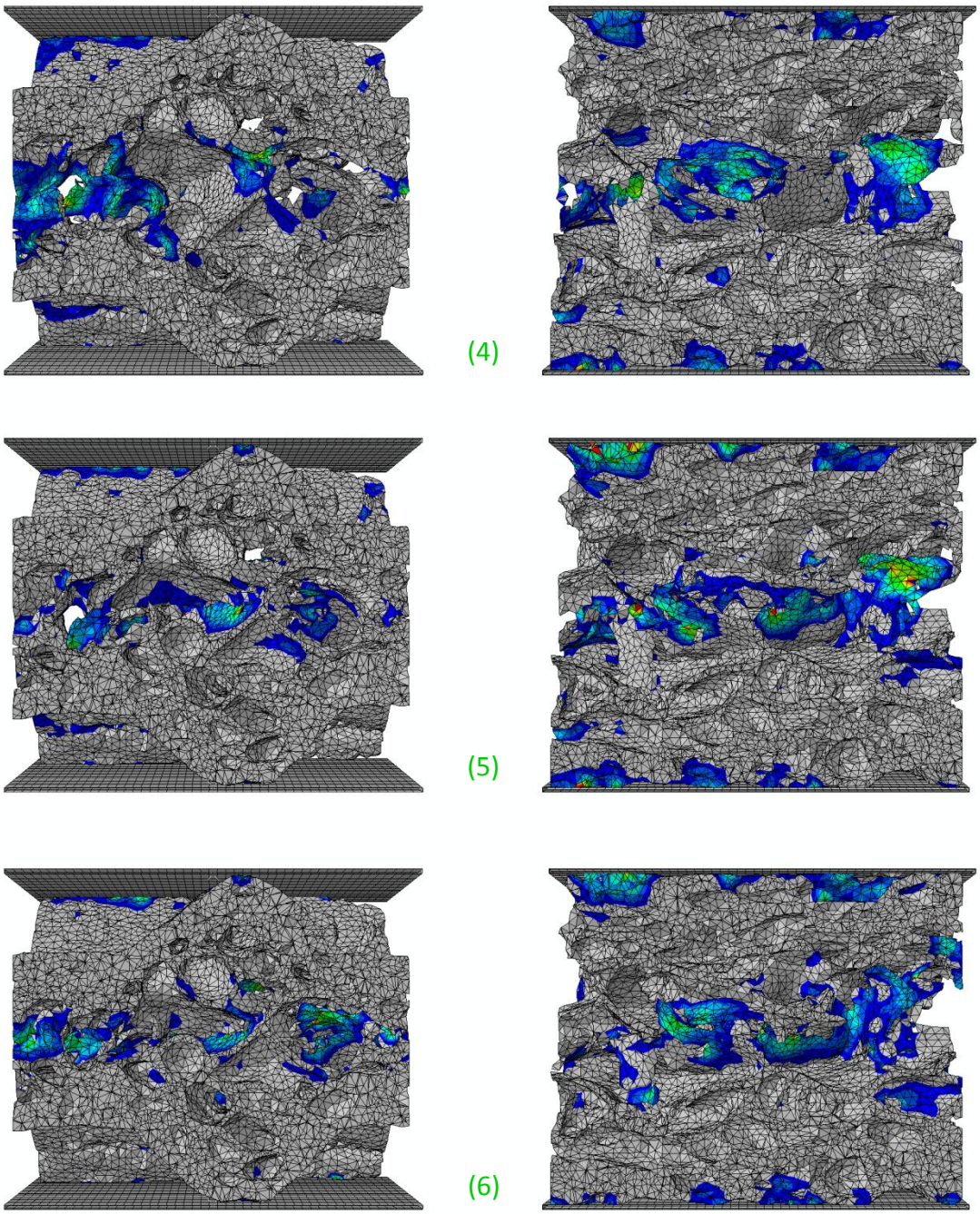

Figure 6.48 The damaged wafer RVE at different stages in the compression

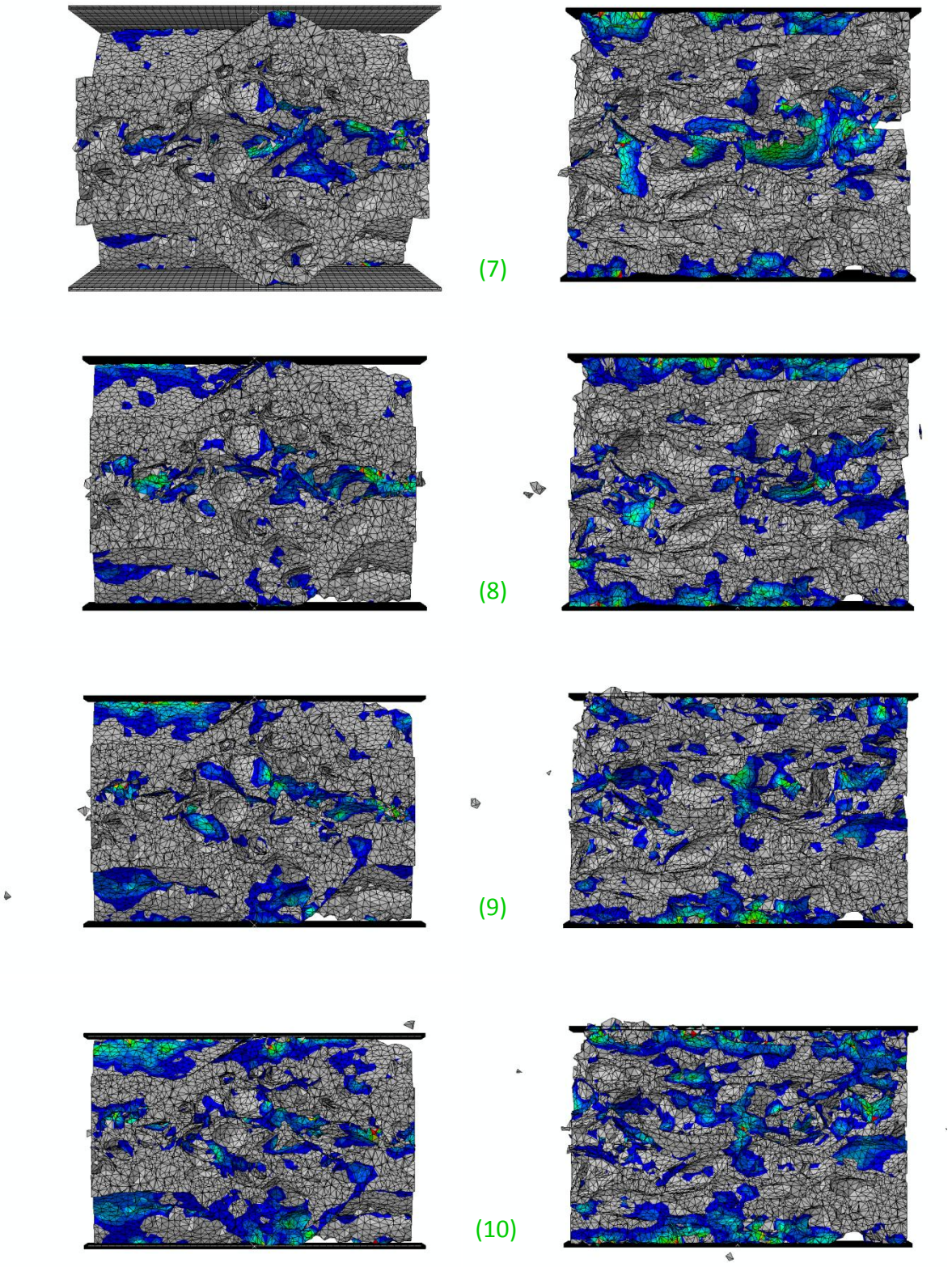

Figure 6.49 The damaged wafer RVE at different stages in the compression

6.4.3. Experimental Verification

The deformation behaviour predicted from the finite element simulation was compared to what was observed experimentally from the in-situ SEM and XMT compression tests. The in-situ SEM tests produced deformation plots which were compared to the FE output in Figure 6.50. Both graphs showed the initial linear deformation followed by a rapid drop in the stress and continued jagged response. As discussed in Chapter 4, the stress-strain curves for the in-situ SEM compression tests were reduced in the stress axis due the influence of the vacuum. This accounts for the difference in the stress values beyond the initial damage. The in-situ XMT compression was static and thus a continuous deformation plot could not be obtained. However at each increment of displacement, the load was recorded on the load cell. At these specific increments of global strain, the values were plotted against the FE output on Figure 6.50. The finite element output and the results obtained from the in-situ experiments were in close agreement to each other which further hinted to the validity of the model.

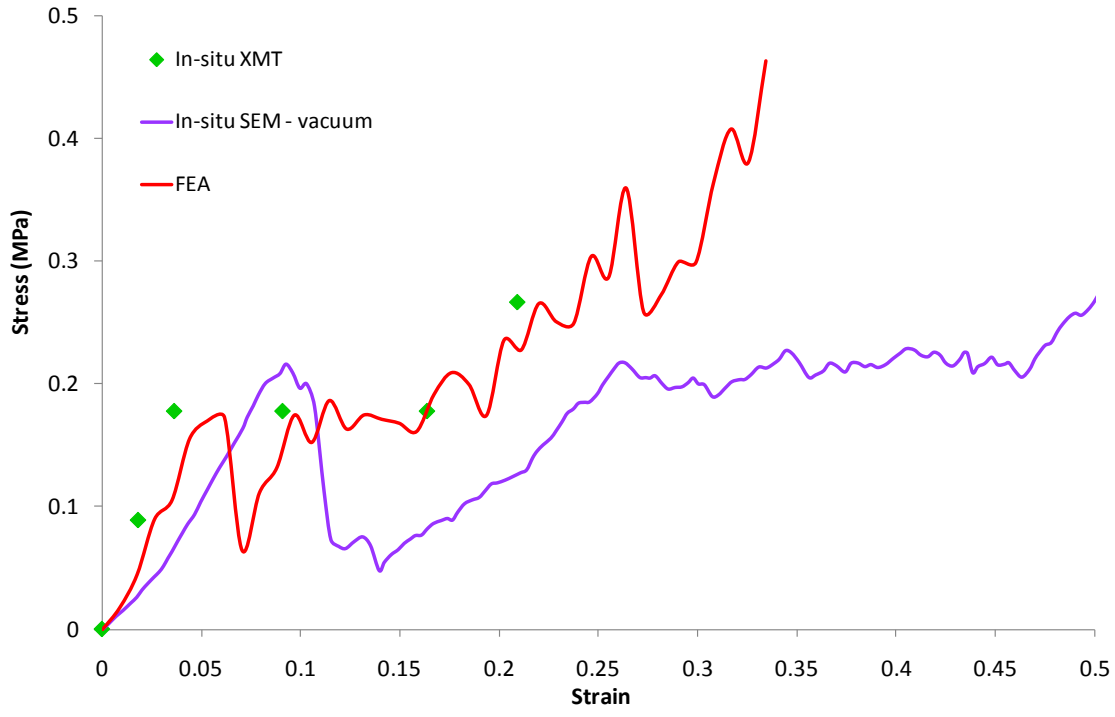

Figure 6.50 Comparison of the finite element output to the in-situ SEM and XMT compression results

It was possible to not only compare the outputs graphically but visually as well in Figure 6.51 and Figure 6.52. The microstructure of the FE, SEM and XMT wafer at specific global strains were analysed. At strains less than 5%, which corresponded to the elastic region, there was no visible fracture in the micrographs nor the tomographic scans. The FE simulation verified this and its contour plot showed that internal stresses were developing within the cell walls of the core. At the onset on initial fracture of the actual cell walls, the stresses within the core of the FE model increased and elements were deleted. Beyond a global strain of 9% the SEM and XMT images showed more cell wall breakage as well as the core collapse. More elements from the simulation progressively deleted and interactions between adjacent cell walls were apparent. The simulation predicted the core being damaged while the denser skins were unaffected, as was seen in the SEM videos and final two tomographic slices. The contour plots showed that the stresses were built up within the core while the skins were relatively stress free. By visual analysis and comparison to the in-situ experiments, it could be seen that the finite element simulation accurately predicted the deformation of the wafer.

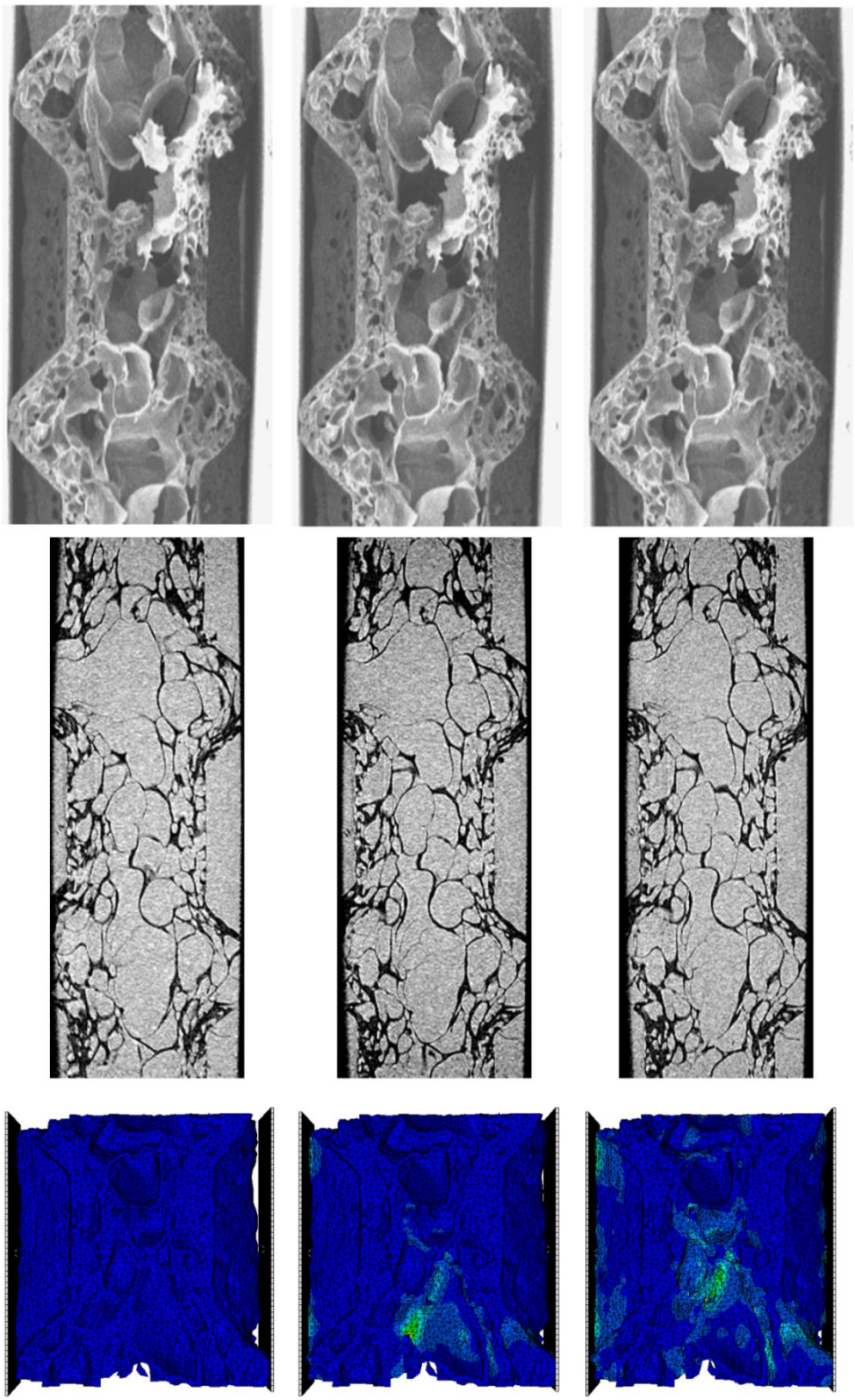

Figure 6.51 Comparison of the wafer structure from FE, XMT and SEM at global strains of a) 0, b) 0.018, c) 0.036

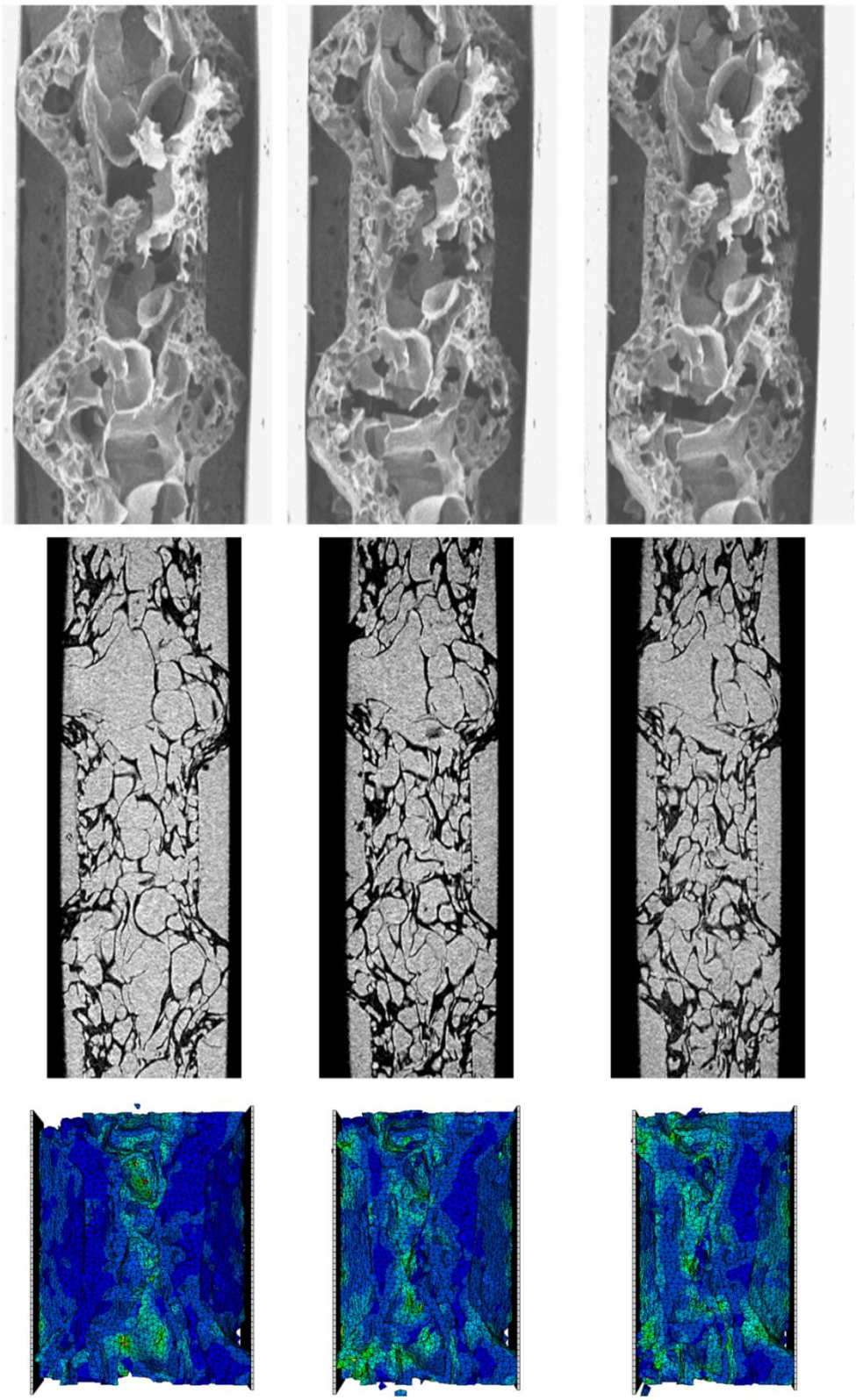

Figure 6.52 Comparison of the wafer structure from FE, XMT and SEM at global strains of a) 0.091, b) 0.164, c) 0.209

6.4.4. Cutting Simulation

The same wafer architecture used for the compression model was used for the cutting simulation. The material model and constants were kept the same as listed in Table 6.1. The blade geometry was represented with rigid elements and was displaced through the wafer in a direction perpendicular to the cross-section. The dimensions of the blade were same as the actual blade used in the experiments of Section 3.4.2 and Section 4.4.8. As with the experiments, the sharp edge was used to cut the wafer along a reeding and between reedings which is shown in Figure 6.53a and Figure 6.53b respectively. However, the wafer model represented only 2.5 mm, unlike the actual specimens which were 12.5mm wide and 25mm long. Symmetrical boundary conditions were applied to the two side faces of the wafer model that were parallel to the blade cutting direction and the face on the opposite side of the blade.

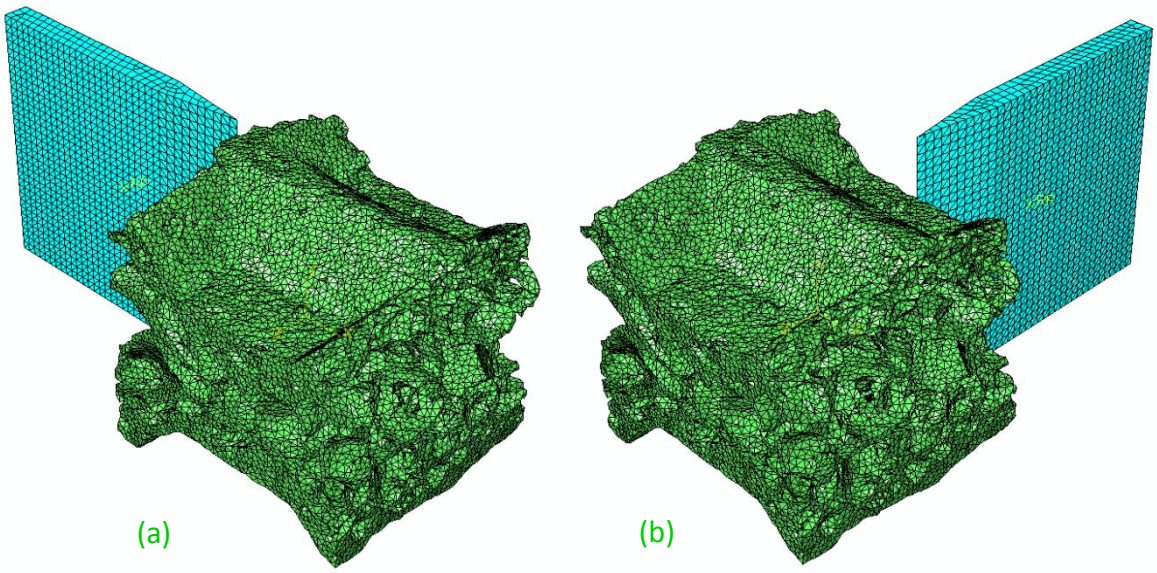

Figure 6.53 The FE models for the cutting simulation a) along a reeding and b) between reedings

As the blade moved through the wafer, elements of the wafer deleted simulating the cutting process. The load-displacement output of the blade for each of the cutting combinations was plotted in Figure 6.54 and compared to the experimentally obtained graphs. The FE output did not match the experimental data in either magnitude or pattern.

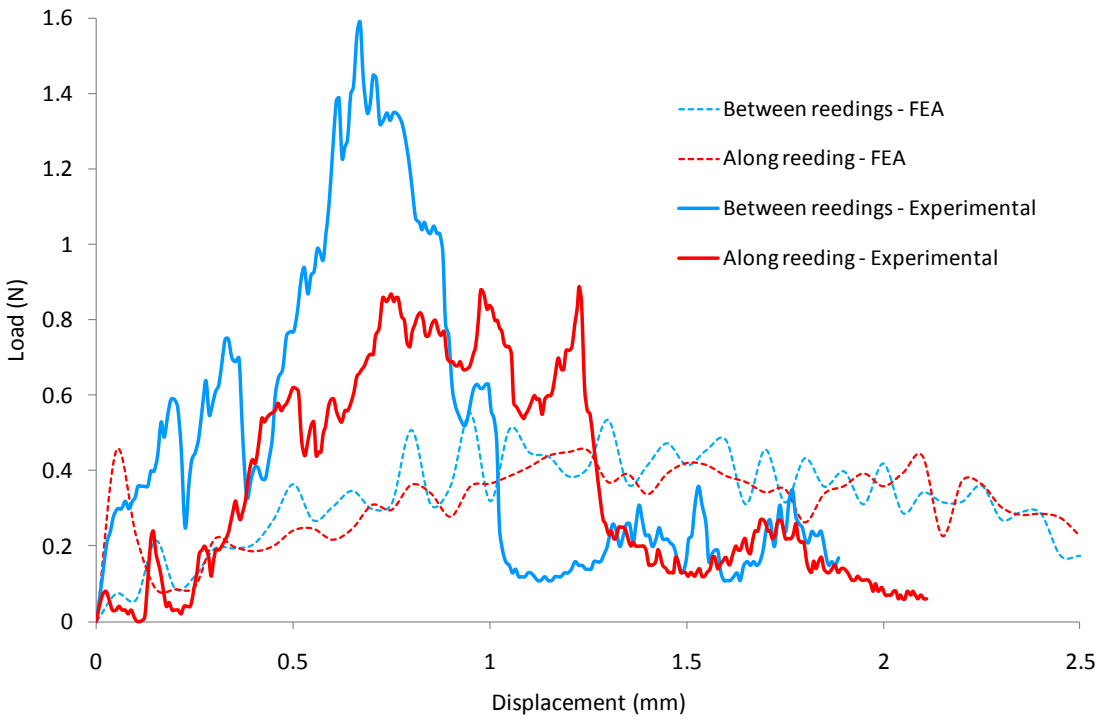

Figure 6.54 Load-displacement plots from finite element simulation and the experimental cutting using the sharp edge of the blade

In the case of the sharp edge, there was no increase in load followed by a sharp drop indicating that there was no crack propagation. The model also displayed no element deletion ahead of the blade tip. Upon visual inspection, it was observed that there were suspended particles in the path of the blade. The blade simply passed through these elements without contacting them. There was no significant difference in either the magnitude or pattern of the load-displacement curves whether the blade passed through the reeding or between reedings.

There were two main possibilities for the disparity between the experimental and numerical results. Firstly, the geometry of the model was only a fraction of the actual specimens used in experiments. Thus the output from the model was not representative of the experiments that were performed. Secondly, the contact interaction implemented in the model was applicable only to the surface of external elements and not on the elements below it. This meant that the rigid body would interact with the top element and if the critical stress was

reached, then the element would delete. However, if the element below it did not reach the critical stress and delete, then the rigid body would not interact with it and thus pass right through it. This phenomenon accounted for the floating elements seen in the wafer cutting model. Since all of the elements in the blade path were not interacting with the rigid blade, this resulted in the reduced magnitude of the load.

The XMT finite element model showed that the compression of the wafer could be simulated to a high degree of accuracy. While the cutting simulations were not comparable to the experimental data, the limitations of the model were noted. These obstacles can be overcome in the future and are discussed in Section 8.6. Thus the finite element method has a strong potential to be used to predicting the deformation response and simulating the cutting process of the wafer.

6.5. Summary

A finite element analysis was conducted on an idealised repetitive geometry of the wafer based on the dimension obtained from optical micrography. The model was partitioned into the skin and core regions, each assigned with the respective modulus values calculated analytically. The crushable foam material model was applied to the core so that the deformation beyond the elastic stage could be modelled. In compression, the model slightly overpredicted the apparent modulus while in bending the model underpredicted the stiffness when compared to the experimental data.

The 3D volume of the wafer reconstructed from the XMT scan was used to generate a tetrahedral meshed grid suitable for finite element analysis. This allowed the actual architecture of the wafer to be modelled with a simple linear elastic material model applied to the elements of the solid wafer. The fracture of the wafer beyond the elastic region was simulated by implementing a damage criterion with element deletion. The damage was initiated by a plastic strain criterion and the damage evolution was governed by a fracture energy. These two parameters were reduced to minimal numerical values so that the damage material model would behave in a brittle manner.

The FE output deformation curve possessed an initial linear region followed by a jagged plateau. The deformation plot from the FE analysis was compared to the experimental stress-strain curves and shown to have quite similar trends. Visually, it could be seen that the maximum stresses initially developed within the core region and followed by element deletion. As the model was further compressed, the broken cell walls of the core interacted with each other due to the contact implemented between elements. The deformation predicted by the FE model was observed experimentally from the in-situ SEM and XMT compression tests. The finite element model predicted the response of the wafer in compression to a high level of accuracy and showed great potential to simulate the cutting process.